Received: 18 November 2018 | Accepted: 21 February 2019

DOI: 10.1002/hyp.13450

RESEARCH ARTICLE

WILEY

Sources and variability of CO_2 in a prealpine stream gravel bar

Kyle S. Boodoo[1,2] | Jakob Schelker[1,2] | Nico Trauth[3] | Tom J. Battin[4] | Christian Schmidt[3]

[1] Department of Limnology and Bio-Oceanography, University of Vienna, Vienna, Austria

[2] EcoCatch, WasserCluster Lunz—Biological Station GmbH, Lunz am See, Austria

[3] Department of Hydrogeology, Helmholtz Centre for Environmental Research—UFZ, Leipzig, Germany

[4] Stream Biofilm and Ecosystem Research Laboratory, ENAC, Ecole Polytechnique Fédérale de Lausanne, Lausanne, Switzerland

Correspondence
Jakob Schelker, Department of Limnology and Bio-Oceanography, University of Vienna, Althanstrasse 14, A-1090 Vienna, Austria.
Email: jakob.schelker@univie.ac.at

Funding information
FP7 People: Marie-Curie Actions, Grant/Award Number: 607150; European Union, Grant/Award Number: 607150

Abstract

Gravel bars (GBs) contribute to carbon dioxide (CO_2) emissions from stream corridors, with CO_2 concentrations and emissions dependent on prevailing hydraulic, biochemical, and physicochemical conditions. We investigated CO_2 concentrations and fluxes across a GB in a prealpine stream over three different discharge-temperature conditions. By combining field data with a reactive transport groundwater model, we were able to differentiate the most relevant hydrological and biogeochemical processes contributing to CO_2 dynamics. GB CO_2 concentrations showed significant spatial and temporal variability and were highest under the lowest flow and highest temperature conditions. Further, observed GB surface CO_2 evasion fluxes, measured CO_2 concentrations, and modelled aerobic respiration were highest at the tail of the GB over all conditions. Modelled CO_2 transport via streamwater downwelling contributed the largest fraction of the measured GB CO_2 concentrations (31% to 48%). This contribution increased its relative share at higher discharges as a result of a decrease in other sources. Also, it decreased from the GB head to tail across all discharge-temperature conditions. Aerobic respiration accounted for 17% to 36% of measured surface CO_2 concentrations. Zoobenthic respiration was estimated to contribute between 4% and 8%, and direct groundwater CO_2 inputs 1% to 23%. Unexplained residuals accounted for 6% to 37% of the observed CO_2 concentrations at the GB surface. Overall, we highlight the dynamic role of subsurface aerobic respiration as a driver of spatial and temporal variability of CO_2 concentrations and evasion fluxes from a GB. As hydrological regimes in prealpine streams are predicted to change following climatic change, we propose that warming temperatures combined with extended periods of low flow will lead to increased CO_2 release via enhanced aerobic respiration in newly exposed GBs in prealpine stream corridors.

KEYWORDS

aerobic respiration, carbon dioxide, gravel bar, hyporheic flow, reactive modelling, temperature

1 | INTRODUCTION

Streams and rivers have been shown to play a significant role in the global carbon cycle (Battin et al., 2009; Raymond et al., 2013), with recent estimates of carbon dioxide (CO_2) evasion fluxes to the atmosphere ranging between 0.65 and 3.9 Pg C $year^{-1}$ (Aufdenkampe et al., 2011; Drake, Raymond, & Spencer, 2017; Lauerwald, Laruelle, Hartmann, Ciais, & Regnier, 2015; Raymond et al., 2013). This more than twofold range in estimates highlights the difficulties in accounting for the inherent spatio-temporal variability of CO_2 outgassing from streams (Peter et al., 2014; Schelker, Singer, Ulseth, Hengsberger, & Battin, 2016) and constraining the contribution of their various CO_2 sources (Hotchkiss et al., 2015; Rasilo, Hutchins, Ruiz-González, & del Giorgio, 2017). Variability in physicochemical and hydrological factors has been found to influence CO_2 concentrations and fluxes within stream corridors: heterotrophic in-stream aerobic respiration (Crawford et al., 2014; Hotchkiss et al., 2015) and hyporheic heterotrophic metabolism (Boulton, Datry, Kasahara, Mutz, & Stanford, 2010; Grimm & Fisher, 1984; Krause et al., 2011; Naegeli & Uehlinger, 1997); direct groundwater inputs of terrestrially derived CO_2 (Crawford et al., 2014; Duvert, Butman, Marx, Ribolzi, & Hutley, 2018; Marx et al., 2017); and the oxidation of CH_4 inputs from groundwater to CO_2 (Hlaváčová, Rulík, Čáp, & Mach, 2006; Rasilo et al., 2017). As a result, there is a need to identify the sources and drivers of spatial and temporal variability in CO_2 production and evasion from stream corridors. This is particularly important in the face of climatic change that will affect stream temperature and discharge.

In-stream bedforms such as riffles and gravel bars (GBs) typically facilitate the downwelling of streamwater into the streambed along a hydraulic gradient between the upstream and downstream ends of the bedform (Trauth, Schmidt, Maier, Vieweg, & Fleckenstein, 2013; Trauth, Schmidt, Vieweg, Oswald, & Fleckenstein, 2015). Upon downwelling, streamwater mixes with the shallow groundwater within the hyporheic zone and undergoes biogeochemical reactions, changing its physical and hydrochemical properties. This may lead to modification of the temperature, as well as concentration of dissolved oxygen (DO), solutes, and nutrients of the water parcel (Grant, Burkholder, Jefferson, Lewis, & Haggerty, 2006; Kasahara & Hill, 2008; Marzadri, Tonina, & Bellin, 2012, 2013; Norman & Cardenas, 2014; Trauth, Schmidt, Vieweg, Maier, & Fleckenstein, 2014; Trauth et al., 2015). The degree of alteration of these characteristics over space and time is typically dependent on the degree of mixing between streamwater and groundwater and the prevailing biogeochemical reactions within the subsurface (Boano et al., 2014; Cardenas & Wilson, 2007; Kasahara & Wondzell, 2003). Physicochemically modified water of the hyporheic zone may upwell, returning to the streamwater at a later time (seconds to days), or contribute to the ambient groundwater, depending on site-specific sediment properties and prevailing hydraulic conditions.

Substantial sections of GBs may remain unsubmerged at mean stream discharge, with shallow subsurface flow occurring within the GB during most of the hydrological year. As a result, GBs can act as a direct interface between the hyporheic zone and the atmosphere. The unsubmerged surface of GBs has been shown to have significantly higher CO_2 evasion fluxes, as compared with the equivalent area of its adjacent stream (Boodoo, Trauth, Schmidt, Schelker, & Battin, 2017). These observed CO_2 evasion flux patterns are similar to those of intermittent streams during periods of flow intermittency versus times of continuous flow (Gómez-Gener et al., 2016; Looman, Maher, Pendall, Bass, & Santos, 2017; von Schiller et al., 2014). To fully understand the role of GBs on the carbon balance of stream corridors, it is thus important to quantify the spatio-temporal variability in the sources and magnitude of CO_2 evasion fluxes.

Here, we combined measured data and model scenarios to disentangle the contribution of the distinct sources of CO_2 within a GB and account for observed spatio-temporal variability in CO_2 concentration and the resultant GB effluxes, across three varying discharge-temperature conditions. Dissolved organic carbon (DOC) acts as the main substrate for aquatic aerobic respiration (Hotchkiss et al., 2015; Lapierre, Guillemette, Berggren, & Del Giorgio, 2013; Ward et al., 2013). Although DOC availability has been hypothesized to control aquatic CO_2 levels, several studies failed to identify a direct relationship (Campeau & Del Giorgio, 2014; Finlay, 2003). To account for these notions, we considered two different DOC concentration scenarios in our model: one representing observed DOC concentrations and one where additional organic carbon (OC), for example, from sediment OC is available for respiration. Accounting for streamwater inputs to the hyporheic zone via downwelling at different temperature-discharge conditions, we further partitioned the major sources of CO_2 within the GB. From this, we determined the spatio-temporal variability in the relative contributions of different sources to overall CO_2 concentration within the bedform. We focused on seasonal baseflow conditions, as it is likely that the extent and intensity of low flows and droughts will increase with continued global warming (Intergovernmental Panel on Climate Change, 2013; Schnitzer et al., 2014). This will likely increase the percentage of stream area covered by exposed GBs and their CO_2 evasion flux (Boodoo et al., 2017). Our results further advance our current understanding of the effect of seasonal discharge and temperature on subsurface aerobic respiration within GBs. They highlight the implications of stream hydraulics—average water residence times and flowpaths, and existing physicochemical conditions, on subsurface respiration and CO_2 evasion fluxes.

2 | STUDY SITE

Our study site was a point GB located in a third-order prealpine stream, the Oberer Seebach (OSB), Lunz am See, Austria (47°51′08″ N, 15°03′54″E, 600 m above sea level), which drains a catchment area of approximately 20 km^2 (Figure 1). The OSB GB is predominantly unsubmerged during the hydrological year and measures ~42 m in length and 8-m width (maximum dimensions) during baseflow. The streambed primarily consists of alluvial sediment, underlain by a low-permeability layer of ancient lake sediment and calcareous rock; median sediment size is 23.1 mm and average porosity 29% (Battin, 1999). The OSB hydrology is typical of low-order prealpine streams,

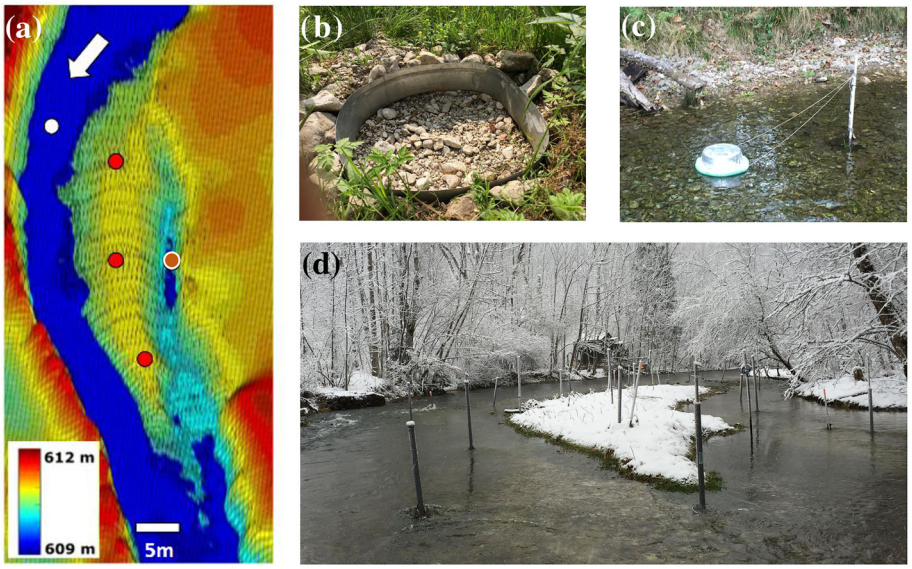

FIGURE 1 (a) Topography of study site and sampling locations for CO_2 and water chemistry. The white arrow denotes flow direction, and coloured circles denote sampling locations of streamwater (white), gravel bar (GB; red), and side channel (brown). (b) GB surface sampling location. The GB armour layer and/or thin (~2–4 cm) layer of fine sediment and plant material was removed to expose the GB more consistently and densely packed sediment, providing an even surface to place CO_2 loggers. (c) Floating streamwater CO_2 chamber near the head of the GB. (d) View of OSB, looking upstream from the GB tail end, showing the main stream channel (left) and active side channel (right)

with a nival flow regime; average discharge is 752 L s^{-1} (2010–2016), with snowmelt peak discharges up to 28,000 L s^{-1}. The OSB subsurface hydrology is mainly influenced by downwelling streamwater, in addition to topographically driven ambient groundwater flows from the steep left-bank hillslope, beneath the stream, and towards the opposite right floodplain (Battin, 1999). A side channel of the OSB stream is separated from the main stream by the upstream section of the GB (Figure 1). During summer baseflow, surface flow along the side channel typically disappears, and isolated pools along the length of the side channel are then maintained by streamwater throughflow via the GB. At above average stream discharges, side channel above surface connectivity with the mainstream is restored. The annual mean OSB streamwater temperature is 6.87 ± 2.07°C (mean ± *SD*, 2010–2016), with streamwater electrical conductivity (EC; 232.4 ± 13.9 µS cm^{-1}) and pH (8.0 ± 0.2), values typical of carbonate streams (Peter et al., 2014).

3 | METHODOLOGY

3.1 | Hydrological, physicochemical, and CO_2 data collection

We based our study on a spatially resolved hydrological and physicochemical dataset acquired by multiple sampling campaigns during different discharge-temperature conditions. Water levels were measured along the GB, within the hillslope groundwater, and within the stream. In the GB, Trutrack® WT-HR 1500 (Tru Track Ltd, Christchurch, NZ, accuracy: ±1 mm) water level probes were placed at 23 locations. In the stream and at the hillslope riparian zone (three locations), water levels were measured by probes from Hydrotechnik GmbH, Limburg, DE (accuracy: <0.05% of measured value). Streamwater and GB hydraulic heads were recorded at 10-min intervals, whereas groundwater heads were recorded every 30 min. We measured CO_2 concentration and evasion fluxes from three locations along the unsubmerged (at discharges ≤ the annual average) section of the GB (head, crest, and tail, Figure 1) and at the streamwater surface, during three separate, 1-week sampling campaigns, using sealed, land-based, and floating CO_2 flux chambers respectively following the design by Bastviken, Sundgren, Natchimuthu, Reyier, and Gålfalk (2015). Additionally, we measured complementary physicochemical properties (temperature, DO, EC, and DOC concentration) of streamwater, GB porewater (measured at 75 and 125 cm below GB crest surface level, d_{75} and d_{125}, respectively), and groundwater. DO and in situ temperature were sampled from the GB piezometers using a dipping probe during the slow extraction of porewater, EC was determined after sample extraction from the GB subsurface on site, and DOC concentration of filtered samples was determined within 48 hr of sampling (Supporting Information Text 1). As the GB side channel contained standing pools of water that may be physicochemically distinct from that of the stream and GB, we also sampled its physicochemistry. Sampling campaigns spanned a range of seasonal low flow discharges and water temperatures: LQ (71 L s^{-1}, 10.2°C), MQ (310 L s^{-1}, 7.5°C), and HQ (478 L s^{-1}, 5.4°C) that were conducted in September 2015, November 2015, and March 2016, respectively (Figure 2). We also conducted two high-resolution topographical surveys. These included mapping of the water perimeter and of hydraulic data of the streamwater–GB–streambank interface,

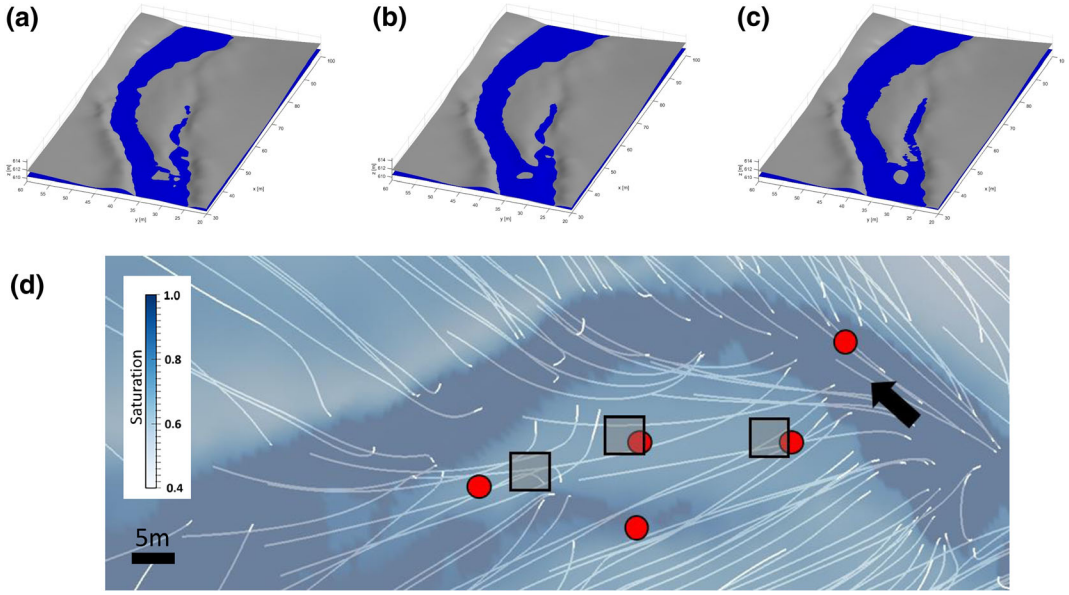

FIGURE 2 Digital elevation model of gravel bar, showing stream wetted perimeter at the three different studied discharge-temperature conditions (a–c) (LQ to HQ). (d) Flowpath of streamwater (white lines) as modelled by particle tracking at baseflow. Squares represent the locations of CO_2 evasion flux and concentration measurements, as well as for modelling of CO_2 evasion fluxes. The red circles show sampling location of porewater at 75- and 125-cm depth below surface. The black arrow indicates the flow direction of streamwater

at known discharges. This allowed for the parameterization of a reactive transport model to estimate GB aerobic respiration and the determination of other residual sources of CO_2 within the GB. Further details of the sampling methods can be found in the Supporting Information Text 1. We estimated groundwater contributions to GB surface CO_2 concentrations on the basis of median estimates of streamwater:groundwater mixing within the upper GB subsurface (d_{75}), using EC as a conservative tracer in endmember mixing analysis (Boodoo et al., 2017). Groundwater endmember CO_2 concentration was estimated as the highest observed CO_2 concentration within the GB per studied condition, similar to Peter et al. (2014).

CO_2 concentrations and fluxes to the atmosphere were measured using flux chambers (Bastviken et al., 2015; Boodoo et al., 2017) positioned along the GBs head, crest, and tail (Figure 1). Using this technique allows to directly measure net atmospheric exchange of CO_2 of the measured surface, as well as concentrations at equilibrium, thereby omitting the need to estimate the gas transfer coefficient. In addition to surface CO_2, streamwater CO_2 concentration was recorded every 3 hr as pCO_2 using a greenhouse gas Sentinel (Axys Technologies, Sidney, BC, Canada) automated sampler (Peter et al., 2014). CO_2 concentration at the GB surface was determined as CO_2 chamber equilibrium concentration, denoted by the asymptote of the CO_2 concentration increase over time. As CO_2 concentration curves and their asymptote could be modelled by logistic regression models, we used the SSlogis logistic regression function from the {stats} package in R (R Core Team, 2017) to derive all measured CO_2 concentrations. The regression model allows the calculation of the initial starting value for the model—the asymptote and gradient, based on the measured input data. We accepted only asymptote values fulfilling the following criteria: average change in CO_2 concentration of $\leq$1.0% over 10 consecutive readings (readings at 2-min intervals) and standard error <5% of the predicted CO_2 concentration. A 1.0% change in CO_2 concentration during our study corresponds to 11–35 ppm. Streamwater CO_2 concentration measurements not coinciding with GB sampling times were estimated from linear interpolation. Measured pCO_2 at 1 atmosphere was converted to CO_2 concentration (ppm) based on the fact that pCO_2 readings were taken using dry air samples (sample passed through desiccant; water vapour in sample is assumed as zero). Corresponding CO_2 evasion flux data were taken from Boodoo et al. (2017).

Overall, 19%, 16%, 8%, and 16% of CO_2 concentration data from the GB head, crest, tail, and streamwater, respectively, were excluded from further analysis. Approximately 50% of all excluded data corresponded to LQ, possibly due to the substantially shorter sampling times during LQ (Supporting Information Text 2). CO_2 data corresponding to the GB head during MQ were excluded from analysis due to atypically low CO_2 evasion flux and concentration values, suggesting leakage of the CO_2 chamber during measurements.

3.2 | Reactive transport modelling

We modelled the steady-state subsurface flow, solute transport, and aerobic respiration reactions within the GB for the three distinct discharge-temperature conditions (Figure 2). The scenarios were based on the site topography, measured stream wetted area, and average hydraulic and physicochemical data for each sampling period. The multicomponent reactive transport modelling code, MIN3P, was used to simulate steady-state variable saturated groundwater flow, solute transport, and in situ biochemical reactions within the GB, with gas

transport modelled according to Fick's law (Mayer, Frind, & Blowes, 2002) and measured streamwater CO_2 concentration used as an input to the model.

3.2.1 | Hydraulic model parameterization

Three individual steady-state groundwater flow models were set up for LQ, MQ, and HQ. The modelling domain spanned 127 m × 83 m × 3.5 m, with horizontal cell dimensions of 0.5 × 0.5 m (Figure 2). Vertical mesh cell resolution decreased with depth, from 0.01 m near the GB surface to a cell height of 0.1 m towards the base of the model according to a quadratic function, giving in total of 637,440 (256 × 166 × 15) mesh cells. The streamwater levels, based on the detailed topographic surveys, were interpolated across the study area and assigned as Dirichlet boundary conditions to the top layer of the groundwater model. At the upstream and downstream lateral boundaries, constant heads were assigned, creating an ambient groundwater flow field below the stream with a gradient of 0.41%, in accordance with the measured OSB stream gradient (Battin, 1999). The absolute values of the upstream–downstream heads were adjusted during the hydraulic model calibration process for each of the three modelling scenarios (see below "calibration procedure"). A no-flow boundary was set at the bottom of the model domain (3.5 m below the average surface of the GB), which corresponds to the position of a low-permeability layer of fine lake sediment and calcareous rock (Battin, 1999). Additionally, no-flow boundaries were assigned along the lateral sides of the modelling domain, parallel to the stream flow direction. Within the model, OSB sediment properties were assumed homogeneous, but anisotropic, with a constant sediment porosity of 0.29 (Battin, 1999). For parameterizing hydraulic conductivity in the horizontal direction (K_h), the geometric mean of the slug tests was used (Chen, 2000)—GB mean: 7.95×10^{-2} cm s^{-1} (Table 1). Hydraulic conductivity within the GB was determined via falling head slug tests and was evaluated utilizing the Hvorslev (1951) method. Water level in the well was measured with an HT Type 255 water level sensor. Vertical hydraulic conductivity (K_z) was determined via calibration of the model (see Section 3.2.4). Model calibration hydraulic parameters are summarized in Table S1.

3.2.2 | Reactive transport model parameterization

Reactive transport for steady-state reactions within the model were calculated as

$$R_s = \nabla\left(\frac{q}{n} C_s - D\nabla C_s\right), \quad (1)$$

where R_s is the kinetic rate (source/sink terms) of the solute species "s," q is the Darcy flux, C_s is the concentration of the species "s," n is the sediment porosity, and D is the hydrodynamic dispersion tensor.

We simulated aerobic respiration of DOC, where 1 mol of O_2 is required to convert 1 mol of carbon (C) to a single mole of CO_2, according to the equation:

TABLE 1 Variability in hydraulic conductivity along the OSB gravel bar

	Head				Crest				Tail				Side channel			
	Min.	Max.	Avg. ± SD	n	Min.	Max.	Avg. ± SD	n	Min.	Max.	Avg. ± SD	n	Min.	Max.	Avg. ± SD	n
Hydraulic conductivity ($m\ s^{-1}$)	2×10^{-4}	8×10^{-4}	$4 \times 10^{-4} \pm 3 \times 10^{-4}$	12	5×10^{-4}	1.8×10^{-3}	$1.1 \times 10^{-3} \pm 5 \times 10^{-4}$	12	4×10^{-4}	1.5×10^{-3}	$9 \times 10^{-4} \pm 4 \times 10^{-4}$	9	2×10^{-4}	2×10^{-4}	2×10^{-4}	3

$$CH_2O + O_2 \rightarrow CO_2 + H_2O. \quad (2)$$

Aerobic respiration kinetics was simulated using a Monod-type formulation, where the carbon-based electron donor is DOC and the electron acceptor is O_2 according to the equation:

$$R = \mu_{max}\left(\frac{C_{DOC}}{K_{DOC} + C_{DOC}}\right)\left(\frac{C_{O_2}}{K_{O_2} + C_{O_2}}\right), \quad (3)$$

where R is the reaction rate, μ_{max} represents the maximum reaction rate (Table 2), C_{DOC} is the concentration of the electron donor, C_{O_2} is the concentration of the electron acceptor, K_{DOC} is the half-saturation constant for the electron donor (DOC), and K_{O_2} is the half-saturation constant for the electron acceptor (O_2, Table 2). In the model, O_2 and DOC sources are assigned at the streambed boundaries as Dirichlet-type boundary conditions, based on measured streamwater concentrations during the three different conditions (Table 2). The physicochemical conditions that potentially affect aerobic respiration according to Equation 2 (pH, HCO_3^-) were determined from existing literature of the OSB (Battin, 1999; Bretschko, 1991a; Peter et al., 2014) and were assigned to the streambed boundaries and the lateral upstream boundary. Within the model domain, pH and HCO_3^- concentrations are calculated. The model assumes an instantaneous equilibrium between the produced CO_2 and HCO_3^- (carbon dioxide and carbonic acid–base equilibrium). The lateral boundaries parallel to the stream and those along the bottom of the domain were set as chemically deactivated.

3.2.3 | Model scenarios

To evaluate the potential dependence of CO_2 evasion fluxes, derived from aerobic respiration on DOC concentration variability, two streamwater DOC scenarios were considered: an observed DOC scenario (1.26 mg L^{-1}), corresponding to the average of all measured GB DOC concentrations, and a high OC scenario (DOC equivalent =

TABLE 2 Parameterization of the reactive transport model MIN3P

Parameters for simulating water flow and solute transport			
Parameter		**Value**	**Data source**
Hydraulic conductivity K (m s^{-1}), x–y direction		7.95×10^{-4}	This study
Hydraulic conductivity K (m s^{-1}), z direction		6.92×10^{-5}	Calibrated
Porosity (–)		0.29	Battin, 1999
Longitudinal dispersivity (m) Transversal horizontal dispersivity (m) Transversal vertical dispersivity (m)		10 1 0.1	Approximated from Gelhar et al. (1992)
Diffusion coefficient, aqueous phase (saturated zone; m^2 s^{-1}) Diffusion coefficient, gaseous phase (unsaturated zone; m^2 s^{-1})		1.0×10^{-9} 1.0×10^{-5}	Cussler, 1997
Rel. permeability and aqueous phase saturation soil hydraulic function van Genuchten—α (m^{-1}) van Genuchten—n (–)		14.5 2.9	Maier et al., 2009
Monod kinetics for solute reactions			
Parameter		**Value**	**Data source**
Half-saturation constant K_{O2} (mmol L^{-1}) Half-saturation constant K_{DOC} (mmol L^{-1})		6.25×10^{-3} 0.107	Gu et al., 2007
Maximum reaction rate of aerobic respiration $\mu_{max,AR}$ (mmol·L^{-1}·day^{-1})		8.64×10^{-2}	Calibrated
Solute concentrations at model boundaries			
Parameter	**Streambed boundary/streamwater/GB surface–air boundary**	**Lateral upstream boundary/ groundwater**	**Data source**
O_2 [mmol L^{-1}] (mg L^{-1})	LQ: 0.314 (10.05) MQ: 0.328 (10.50) HQ: 0.336 (10.75)	0	This study
Saturated cells HCO_3^- [mmol L^{-1}] (mg L^{-1})	1.918 (117)	1.918 (117)	Bretschko, 1991a
GB surface–air boundary: CO_2 (ppm)	400	—	
DOC (mg L^{-1})	LQ: 1.26 MQ: 1.27 HQ: 1.24	0	This study
pH (–)	8.0	8.0	Battin, 1999; Bretschko, 1991a; Peter et al., 2014

Abbreviations: DOC, dissolved organic carbon; GB, gravel bar.

6.0 mg L^{-1}), accounting for potential additional DOC or particulate OC sources. Variability in average DOC concentration per location (head, crest, and tail) and sampling depth (d_{75} and d_{125}) was not significantly different across the three different sampling periods (pairwise Wilcoxon, $p > .05$, $n = 6$, for all comparisons—p values, Bonferroni corrected).

We assumed that the entire DOC pool is readily available for aerobic respiration reactions. As temperature affects reaction rates and diffusion/dispersion coefficients, via Arrhenius" and Fick's law, respectively, the average (mean of GB head, crest, and tail) GB subsurface temperature was taken into consideration for each of the three conditions (LQ, MQ, and HQ). The spatial temperature variation between streamwater, GB locations, and groundwater was relatively small for each of the scenarios. As a result, the model was parameterized using the spatial median GB (head, crest, and tail) temperature for each of the three discharge conditions. Temperatures were assumed to be homogeneous throughout the model domain. In order to separate the contribution of aerobic respiration from that of downwelled streamwater, in terms of CO_2 concentration and evasion flux at the GB surface, we modelled a third, "conservative" scenario in which the aerobic respiration reaction was turned off, enabling a pure conservative transport of the hydrochemical species. CO_2 concentrations and evasion flux modelled at the surface of the conservative model represent the effective streamwater CO_2 evasion flux from the GB surface under the existing physicochemical characteristics and an air concentration of 400 ppm above the GB surface. We assumed no loss of dissolved CO_2 upon downwelling for the calculation of the streamwater component contribution to overall GB CO_2 concentrations.

3.2.4 | Model calibration

Model calibration comprised a two-step process. First, hydraulic heads within the GB were calibrated. This was followed by calibration of reactive transport parameters towards measured DO saturation. Hydraulic heads for each discharge-temperature condition were manually calibrated towards the measured GB subsurface values (23 locations) by incrementally adjusting both the vertical hydraulic conductivity (K_z) and the absolute upstream and downstream hydraulic heads, while maintaining a constant gradient, corresponding to the stream slope (0.41%; Battin, 1999). This process was repeated to achieve a single K_z, which was valid for all three conditions, whereas upstream and downstream hydraulic heads for each condition (LQ, MQ, and HQ) varied.

Reactive transport was calibrated by matching the measured mean DO saturation within the GB saturated zone at two depths (d_{75} and d_{125}) across the three GB sampling locations (head, crest, and tail) under the three different discharge-temperature conditions. DO calibration involved the utilization of a single maximum aerobic respiration reaction rate (μ_{max}) according to the Monod kinetics (Equation 3), valid for all three conditions (LQ, MQ, and HQ) in the determination of the modelled DO saturation levels. Thus, a total of six DO saturation calibration points (three GB locations over two depths) for each of the three discharge-temperature scenarios could be used. Table 2 summarizes model input variables and parameters for the MIN3P model applied to the GB.

3.2.5 | Particle tracking and calculation of mean water age

We utilized advective particle tracking to determine the flowpaths and ages of the subsurface water below the GB under steady-state conditions, for each of the three seasonal conditions. We estimated mean flowpath lengths and water ages for the two sampling depths corresponding to the point of measurement of CO_2 at the GB surface (head, crest, and tail), in addition to the variability in mean age over the entire depth of the model as water age. Water age was calculated as the average age of all flowpaths passing through a single vertical profile beneath each GB sampling location. Particle tracks were calculated using the open-source visualization software ParaView, version 4.1.0 (Ayachit, 2015), based on a fourth- and fifth-order Runge–Kutta integration of the steady-state porewater velocity fields. Forward particle tracking was used to evaluate the general flow field (losing and gaining, and hyporheic flowpaths) within the GB by releasing four particles per mesh cell over the entire wetted streambed area. Thus, the number of particles released per simulation increased with wetted streambed area—discharge and degree of GB submergence (3,898 [LQ], 4,462 [MQ], and 5,306 [HQ]). Forward particle tracks were flux weighted, and their median residence time, distribution, and orientation within the subsurface were determined. Backward particle tracking was used for identification of streamwater infiltration locations reaching the GB subsurface at head, crest, and tail by releasing particles vertically arranged over the saturated model depth, at the three locations of interest, with a total of 141 particles, at each discharge. We also investigated the potential effectiveness of the modelled OSB stream corridor for DOC removal, quantifying the sources and sinks of the CO_2 over the model domain.

We calculated average streamwater downwelling flowpath velocities as the quotient of flowpath length and water age, corresponding to the GB depths d_{75} and d_{125} at the GB head, crest, and tail and at the side channel. Further, we tested for significant differences between the sampling locations and temperature-discharge conditions via one-way analysis of variance (ANOVA) followed by Tukey's honestly significant difference post hoc tests to identify individual site differences. Unless otherwise indicated, statistical results refer to these post hoc test results. All post hoc p values were Bonferroni corrected for multiple comparisons. Significant differences between the sampling depths d_{75} and d_{125} and modelled CO_2 concentrations under the two modelled scenarios were tested using the Student's t tests. All statistical tests were conducted in R 3.3.3 and SigmaPlot 12.5 in accordance with normality, equal variance, and other test-specific assumptions. We used standard parametric statistical test (t test, one-way and two-way ANOVAs) if assumptions were met; nonparametric tests (such as Mann–Whitney rank test) were applied if nonnormality was present. To test correlations between variables, Pearson's correlation analysis was applied.

4 | RESULTS

4.1 | Physicochemical characteristics of GB porewater and streamwater

GB porewater and streamwater physicochemical characteristics varied both spatially and temporally. DO saturation measured within the streamwater and at the three GB locations (average of d_{75} and d_{125}) increased from LQ towards HQ (Table 3). GB DO saturation significantly varied among locations for all three sampling periods and was consistently higher below the crest, compared with head and tail (Bonferroni-corrected *t* tests, $p < .001$ for all comparisons, $n = 14–21$). Conversely, EC decreased across the sampling seasons from LQ to HQ and significantly varied among locations for all three sampling periods, with the lowest EC consistently measured at the crest (Bonferroni-corrected *t* tests, $p < .001$ for all comparisons, $n = 14–21$). Overall, GB side channel porewater (Figure 1) showed significantly higher EC and lower DO saturation (Bonferroni-corrected *t* tests, $p < .001$, $n = 14–21$), compared with both the streamwater and the porewater below the GB at all three locations (Supporting Information Text 3). Similarly, porewater temperature below the GB and side channel significantly differed between LQ and HQ (ANOVA, $p < .001$, $n = 13$ and 21, respectively). During LQ, temperature at the head of the GB was significantly higher than at the GB crest and side channel ($p < .05$, $n = 13$), whereas during HQ, temperature at the head of the GB was significantly lower than all other locations ($p < .001$, $n = 21$). Streamwater DOC concentrations did not significantly vary between the three studied conditions (Boodoo et al., 2017). DOC average seasonal concentration was highest in both the stream and GB (average of GB head, crest, and tail) during MQ. DOC concentrations within the GB and side channel significantly varied during LQ and HQ (ANOVA, $p < .001$, $n = 13$ and 21 for LQ and HQ), but not during MQ (ANOVA, $p = .09$, $n = 19$).

4.2 | Measured CO_2 concentrations and fluxes

GB surface CO_2 concentration, averaged over the head, crest, and tail, was significantly higher (1.96, 1.54, and 1.59 times) than that of streamwater (Mann–Whitney rank test, $p < .001$ for all comparisons) during LQ, MQ, and HQ, respectively (Figure 3). Streamwater CO_2 concentration temporal variability (measured as the coefficient of variation) decreased from LQ towards HQ. Similarly, the coefficient of variation throughout the GB surface (at the GB head, crest, and tail) was lowest during HQ. Streamwater average CO_2 concentration over each sampling condition was similar during LQ (855 ppm) and MQ (873 ppm) and substantially lower during HQ (762 ppm). Meanwhile, mean CO_2 concentrations per sampling condition also varied over time at all locations along the GB (head, crest, and tail), showing a distinct decreasing pattern from LQ towards HQ. The GB tail showed a consistently higher CO_2 concentration than the more similar head and crest (Figure 3, Table 3), with differences in spatial variability between sampling locations decreasing from LQ to HQ.

Similar to concentrations, CO_2 evasion fluxes measured at the GB surface were significantly higher than those measured from streamwater (Boodoo et al., 2017). CO_2 concentration and evasion fluxes typically decreased from LQ towards HQ. Both CO_2 concentrations and evasion fluxes measured at the GB head were significantly different across the different GB locations (head, crest, and tail) and streamwater, and across the different sampling conditions (LQ, MQ, and HQ), with a significant interaction between location and sampling condition (two-way ANOVA, $p < .001$, for both sampling condition and location and their interaction). Post hoc analyses (multiple *t* tests, Bonferroni corrected for multiple comparisons—Tables S3 and S4) revealed that seasonal variation in CO_2 concentration was significant between LQ:HQ ($p < .05$) and LQ:MQ ($p < .001$), but not between MQ and HQ ($p = .08$). Similarly, CO_2 evasion fluxes were significantly different between LQ:MQ and LQ:HQ only (both, $p < .001$), but not between MQ and HQ ($p = .42$). All comparisons of CO_2 concentrations among the different locations were significant ($p < .001$ for all comparisons, except crest:head where $p < .05$). Only the GB tail CO_2 evasion flux was significantly different from the other GB locations (head and crest) and streamwater ($p < .001$ for all comparisons)

Post hoc analysis of the interaction between location and discharge-temperature conditions for different locations over the same sampling conditions (Tables S3 and S4) revealed several significant differences, particularly related to the GB tail, which was significantly higher than all other tested locations within any single season (except that of the GB head during HQ). Additionally, streamwater CO_2 concentration was significantly lower than all GB locations across each sampling condition (with the exception of the GB head during LQ and MQ; Table S3). Analysis of CO_2 concentration variation per location across different sampling conditions revealed limited significant differences, with only CO_2 concentrations at the GB tail (LQ:tail–HQ:tail and MQ:tail–HQ:tail) being significantly different over seasons (Table S3). Whereas the CO_2 concentration at the GB crest was not significantly different across the different sampling conditions, CO_2 evasion flux at the GB crest was significantly different across all three discharge-temperature conditions. Similar to CO_2 concentration variability, CO_2 evasion fluxes were significantly higher at the GB tail than at the stream and the rest of the GB ($p < .01$ for all comparisons) across all sampling conditions (Table S4).

4.3 | Calibration of reactive transport model against measured hydraulic heads and DO

We calibrated the reactive transport model using measured physicochemical and hydraulic data for the three modelled scenarios. The best match between measured and modelled hydraulic heads in the GB was achieved utilizing a vertical hydraulic conductivity (K_z) of 6.92×10^{-3} cm s^{-1}, with corresponding Nash–Sutcliffe efficiencies of 0.68, 0.76, and 0.87 for LQ, MQ, and HQ, respectively (Figure S1). The calibrated K_z was one order of magnitude lower than the measured K_h (7.95×10^{-2} cm s^{-1}), resulting in an anisotropy ratio (K_h:K_z) of 11.49 (Table S1). The best match μ_{max} between measured and modelled DO data

TABLE 3 Seasonal physiochemical variables and modelled mean hydraulic properties within the OSB stream, side channel, riparian groundwater, and gravel bar over the three discharge-temperature conditions

		LQ			MQ			HQ		
Variable	**Location**	**Mean**	***SD***	**C.V. (%)**	**Mean**	***SD***	**C.V. (%)**	**Mean**	***SD***	**C.V. (%)**
CO_2 evasion flux (mg C·m^{-2}·hr^{-1})	Streamwater	24.06	10.32	42.91	22.83	11.97	52.44	13.89	6.36	45.75
	Head	51.33	32.64	63.6	8.89[a]	5.18[a]	58.34[a]	15.16	5.03	33.14
	Crest	39.49	15.62	39.56	22.22	6.53	29.37	12.79	3.28	25.64
	Tail	51.16	13.47	26.33	37.43	14.51	38.77	36.97	7.08	19.16
CO_2 concentration (ppm)	Streamwater	855	315	36.87	873	223	25.54	762	155	20.30
	Head	1,404	418	29.75	979[a]	150[a]	15.33[a]	1,188	205	17.25
	Crest	1,442	268	18.56	1,358	337	24.83	1,174	113	9.64
	Tail	2,124	315	14.84	1,671	469	28.07	1,292	110	8.55
Temperature (°C)	Streamwater	9.64	0.74	7.7	7.47	0.51	6.89	6.53	0.64	9.85
	Groundwater	12.16	0.14	1.12	8.6	0.07	0.81	4.82	0.9	18.65
	Head (d_{75})	10.71	0.47	4.39	7.29	0.47	6.44	4.39	0.45	10.33
	Crest (d_{75})	10.24	0.42	4.08	7.87	2.33	29.6	5.34	0.51	9.51
	Tail (d_{75})	10.5	0.46	4.35	7.58	0.58	7.65	5.82	0.43	7.47
	Side ch. (d_{75})	9.84	0.25	2.50	7.58	0.44	5.85	5.83	0.45	7.74
	Head (d_{125})	10.25	0.42	4.13	7.42	0.44	5.91	4.79	0.62	12.95
	Crest (d_{125})	9.86	0.45	4.52	7.54	0.51	6.79	6.06	0.44	7.26
	Tail (d_{125})	9.87	0.18	1.8	7.55	0.48	6.4	5.97	0.45	7.55
	Side ch. (d_{125})	9.69	0.18	1.81	7.66	0.40	5.21	6.07	0.30	4.99
DOC (mg L^{-1})	Streamwater	1.26	0.16	12.92	1.27	0.13	10.29	1.24	0.09	7.48
	Groundwater	8.38[b]	3.98[b]	47.47[b]	3.63	0.57	15.6	3.06	0.23	7.39
	Head (d_{75})	1.51	0.34	22.64	1.48	0.17	11.3	1.33	0.1	7.5
	Crest (d_{75})	1.24	0.1	8.05	1.42	0.34	24.17	1.29	0.19	15.01
	Tail (d_{75})	1.62	0.47	29.14	1.68	0.51	30.47	1.31	0.09	7.14
	Side ch. (d_{75})	1.85	0.32	0.02	1.52	0.28	0.02	1.41	0.11	0.01
	Head (d_{125})	1.33	0.16	11.77	1.3	0.14	10.84	1.32	0.1	7.47
	Crest (d_{125})	1.32	0.25	18.6	1.42	0.29	20.75	1.29	0.13	9.99
	Tail (d_{125})	1.32	0.19	14.24	1.4	0.16	11.15	1.25	0.08	6.6
	Side ch. (d_{125})	1.64	0.35	0.02	1.41	0.15	0.01	1.40	0.17	0.01
Dissolved oxygen (%)	Streamwater	110.97	7.40	6.69	116.05	6.18	5.35	118.7	5.08	4.24
	Groundwater	0.44	1.32	300	6.51	5.85	90.56	26.17	10.27	39.58
	Head (d_{75})	49.47	11.81	23.79	69.12	19.32	27.89	93.52	7.29	7.76
	Crest (d_{75})	97.94	5.52	5.63	108.21	4.09	3.73	113.95	4.2	3.65
	Tail (d_{75})	50.9	13.47	26.39	70.78	12.48	17.59	101.47	12.59	12.38
	Side ch. (d_{75})	0.29	1.05	360.56	6.30	2.36	37.48	2.79	2.18	78.20
	Head (d_{125})	73.20	7.07	9.61	88.44	11.15	12.62	78.01	6.18	7.16
	Crest (d_{125})	94.85	6.96	7.33	103.02	3.75	3.64	106.88	7.62	7.1
	Tail (d_{125})	71.33	5.85	8.17	83.47	8.61	10.35	98.27	6.96	7.05
	Side ch. (d_{125})	41.93	3.43	8.19	35.55	6.32	17.79	30.94	3.52	11.39
Electrical conductivity (μS cm^{-1})	Streamwater	253	2.82	1.12	249	3.54	1.42	233	1.93	0.83
	Groundwater	429	47.7	11.13	442	19.98	4.52	361	5.99	1.66
	Head (d_{75})	266	4.43	1.67	266	8.42	3.17	240	4.96	2.07
	Crest (d_{75})	253	3.7	1.46	250	3.42	1.37	234	2.34	1
	Tail (d_{75})	270	5.94	2.2	261	9.59	3.67	234	2.06	0.88
	Side ch. (d_{75})	301	15.02	4.98	279	2.55	0.91	262	6.29	2.39
	Head (d_{125})	257	4.07	1.58	255	3.03	1.19	238	2.98	1.25
	Crest (d_{125})	254	3.17	1.25	251	3.26	1.3	234	2.16	0.92
	Tail (d_{125})	260	2.87	1.11	255	5.24	2.05	236	1.49	0.63
	Side ch. (d_{125})	267	3.42	1.28	266	2.50	0.94	257	6.09	2.37
Variable	Depth	Head	Crest	Tail	Head	Crest	Tail	Head	Crest	Tail
Flowpath velocity (m day^{-1})	d_{75}	2.78	1.28	0.39	3.34	1.78	0.87	3.29	2.03	2.39
	d_{125}	3.52	1.91	0.68	3.26	2.27	1.43	2.98	2.35	1.92
Mean flowpath age (days)	d_{75}	1.45	2.56	3.11	1.23	1.87	1.56	0.89	1.98	0.67
	d_{125}	1.37	1.97	2.51	1.47	1.76	1.29	1.16	2.17	1.48
Mean flowpath length (m)	d_{75}	4.05	3.27	1.20	4.12	3.33	1.36	2.91	4.04	1.61
	d_{125}	4.81	3.77	1.70	4.80	3.99	1.84	3.46	5.11	2.85

Note. Gravel bar (GB) values represent the average of head, crest, and tail over two sample depths (75 and 125 cm below GB surface). Physicochemical variables are averages and standard deviations, obtained from diurnal data. Flowpath age and length represent average modelled values at the two sample depths, respectively. GB side channel data are not shown. The upper section of the table was adapted from Boodoo et al. (2017).

Abbreviations: C.V., coefficient of variation; DOC, dissolved organic carbon.

[a]Data uncertain due to leak in CO_2 flux chambers during sampling.

[b]DOC concentrations for the groundwater station during LQ were exceptionally high and variable and deemed unreliable due to the sampling of a stagnant well.

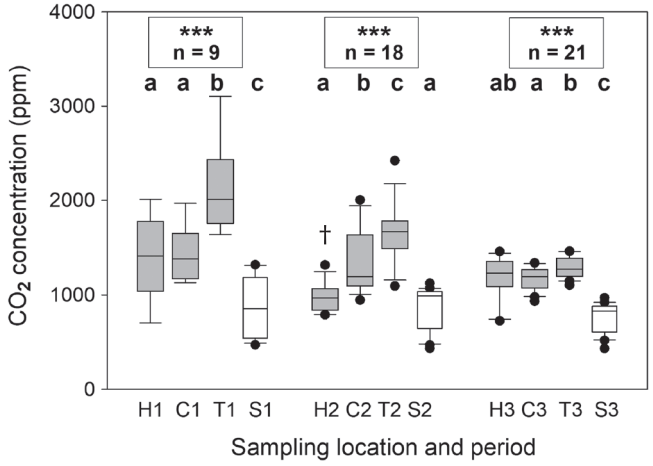

FIGURE 3 (a) Spatial and flow-dependent variability in CO_2 concentration measured at three locations along the gravel bar surface (H, head; C, crest; T, tail, coloured in grey) and at the streamwater surface (S, coloured in white) during different sampling conditions (LQ, MQ, and HQ). Letters above the boxes denote significant differences among locations given the same Q, where locations that are not significantly different from each other share the same letter assignment. Stars indicate significant differences between the mean of all gravel bar locations (the three grey boxes) and that of streamwater (the white box), per sampling condition, with significance levels: $^{*}p < .05$; $^{**}p < .01$; $^{***}p < .001$); *n* is the number of samples. †Data uncertain due to leak in CO_2 flux chambers during sampling

for the high and observed carbon source scenarios was found to be 1.31 and 26.44 mg $C{\cdot}L^{-1}{\cdot}day^{-1}$, respectively. The maximum reaction rate applied under the high OC scenario (1.31 mg $C{\cdot}L^{-1}{\cdot}day^{-1}$) closely matched previously measured rates for the OSB: 1.28 mg $C{\cdot}L^{-1}{\cdot}day^{-1}$ (4.5 mmol $C{\cdot}m^{-2}{\cdot}hr^{-1}$, converting to daily rate and from areal rate to volumetric rate, assuming an aquifer depth of 3.5 m and n = 0.29; Battin, 1999). Modelled DO was within a maximum deviation of 20% of measured DO for most of the sample points, over the different conditions (Figure 4), and was constantly underestimated for HQ under both DOC concentration scenarios. DO saturation at the GB head was best simulated by the model, whereas the model generally overestimated DO saturation at the tail and underestimated at the GB crest (Figure 4). Deviations from observed DO would only have a minor influence on the respiration rate (R, Equation 3). A 50% underestimation of DO concentration would result in ~2% decrease of the respiration rate providing all other parameters remain constant.

4.4 | Flow patterns and water age within the GB

The flow model revealed the OSB stream to be consistently losing across all three Q conditions. Averaged water age across all flowpaths simulated at d_{75} and d_{125} decreased from 2.16 days (LQ), to 1.53 days (MQ), towards 1.39 days (HQ; Table 3). Water age at d_{75} was higher than that at d_{125}, across all locations for each sampling condition.

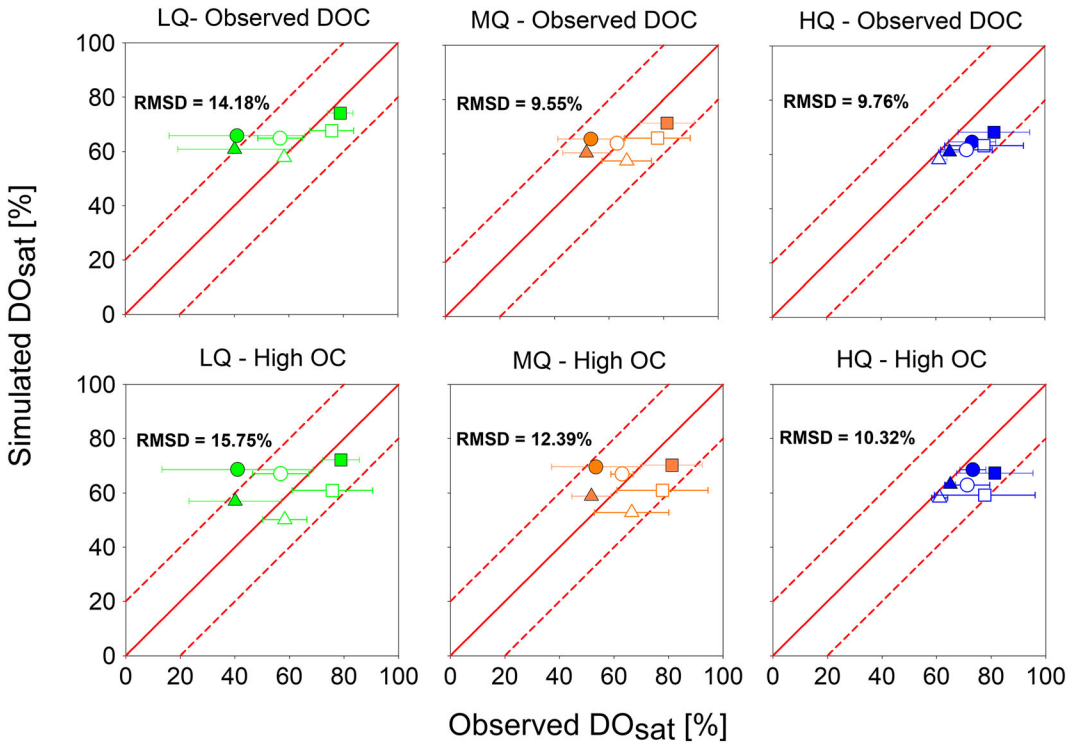

FIGURE 4 Model fit of oxygen saturation within the gravel bar (GB) over the range of discharge-temperature conditions (LQ, MQ, and HQ) for the observed dissolved organic carbon (DOC; upper row) and high organic carbon (OC; lower row) supply. Symbols denote different GB locations (head—circle, crest—square, and tail—triangle) over two depths below the GB surface (filled symbols: d_{75}; empty symbols: d_{125}). Horizontal error bars represent the range of measured dissolved oxygen (DO) values over each individual discharge-temperature condition. MPE denotes the overall model mean percentage error of measured and modelled data for each condition and location. Dashed lines show a 20% deviation from the 1:1 line (solid line) for easier visualization of deviations. RMSD, root mean squared deviation

Overall, at depths >d_{125}, water age generally increased with depth, with the exception of the tail during LQ (Figure 5). The tail of the GB showed a considerably older water age across most of its depth profile during LQ and HQ, compared with the head and crest, which showed near identical age characteristics with increasing depth (Figure 5).

Average GB flowpath length near the surface of the GB only increased slightly from 3.14 m at LQ, to 3.24 m at MQ, towards 3.32 m at HQ. Flowpath length within the upper section of the GB tail was consistently shorter than at the GB head and crest. Subsurface GB CO_2 concentration was significantly correlated to modelled average flowpath age at d_{75} (Pearson's correlation: r = .68, p < .05, n = 9), whereas flowpath age at d_{125} was not significantly correlated to CO_2 concentrations measured at the GB surface (r = .50, p = .17, n = 9).

The average flowpath velocities at d_{75} and d_{125} increased from LQ towards HQ (Table 3). Flowpath velocities generally decreased from the GB head towards its tail. Furthermore, throughout the GB, flowpath velocities towards d_{75} were lower than those to d_{125} during LQ, and higher during HQ, with the exception at the GB crest, where flowpath velocities at d_{75} were consistently lower than d_{125}. Flowpath velocities at the GB tail were notably lower than all other locations during LQ and MQ, becoming more similar to the other GB locations during HQ (Table 3). An analysis of the source locations of downwelled water revealed that during LQ, the GB tail received contributions from the main stream and the side channel (Figure 5).

4.5 | Modelled CO_2 transport

Although both CO_2 evasion flux and concentrations are outcomes of the MIN3P model, here, we focus on model CO_2 concentrations. This

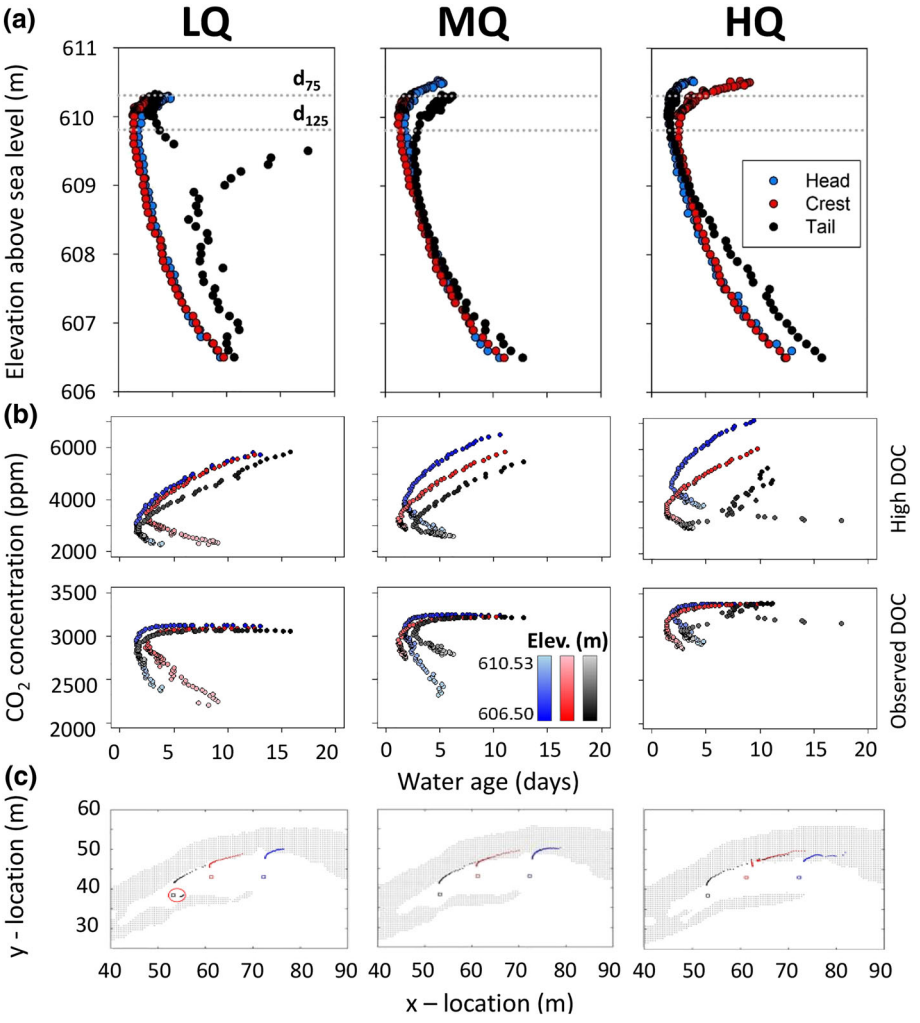

FIGURE 5 (a) Distribution of downwelled streamwater age with depth within the gravel bar (GB) under HQ, MQ, and LQ. Each point represents the average modelled water age of all flowpaths contributing to the specific location. Grey dashed lines, d_{75} (610.31 m) and d_{125} (609.81 m), correspond to the depths at which GB porewater was sampled. (b) Change in modelled CO_2 concentrations with increasing water age for the high organic carbon and observed organic carbon scenarios (upper and lower row, respectively). Points are coloured by location: head (blue), crest (red), and tail (black), with colour intensity depicting elevation as presented in (a) (lighter colours show points closer to the surface). (c) Points of entry of streamwater into the subsurface as modelled by particle back-tracking for flowpaths to the studied GB locations (head—blue, crest—red, and tail—black) during HQ, MQ, and LQ (left to right, respectively). Grey shading denotes wetted stream perimeter. It should be noted that some flowpaths towards the tail of the GB also originate from the side channel during LQ (highlighted red circle). DOC, dissolved organic carbon

allows not only CO_2 source partitioning but also the spatial distribution of CO_2 concentration throughout the GB depth and the influence of travel time to be determined facilitating a more mechanistic understanding of the influence of hydrology on GB CO_2 concentration over space and time.

Modelled CO_2 concentrations within all scenarios increased rapidly with depth within the unsaturated zone of the GB, albeit at varying rates, slowing upon transition to the saturated zone (Figure 6). In the saturated section of the GB, increases in CO_2 concentration with depth under the conservative scenario were negligible. Thus, any deviations from this baseline could be attributed to aerobic respiration. Under the observed DOC scenario, modelled CO_2 concentrations tapered off within the first ~2 m, increasing only slightly with depth thereafter. Under the high OC scenario, CO_2 concentrations continuously increased with depth. CO_2 concentrations in the high OC scenario consistently exceeded those under the observed DOC scenario throughout the model depth, with the exception of the upper section of the GB tail at all Q conditions and at the head under HQ (Figure S2).

CO_2 concentration in the subsurface water increased from the head towards the tail of the GB (Table 4). Furthermore, spatial variation of CO_2 originating from aerobic respiration, measured as the coefficient of variation, decreased with decreasing temperature and increasing discharge, from LQ (24.5%) through MQ (14.6%) towards HQ (5.3%). There was no significant difference between modelled CO_2 evasion fluxes at the GB head, crest, and tail across all sampling conditions under the two DOC scenarios (*t* test: $n = 9$, $p = .634$). Furthermore, simulated CO_2 concentrations at the GB surface and at d_{75} and d_{125} (of the GB head, crest, and tail) did not significantly vary between the two DOC scenarios (*t* test, $p > .05$, $n = 9$), whereas CO_2 concentrations were significantly different at the base of the model (*t* test, $p < .001$, $n = 9$).

Over the different sampling locations and across all three hydrological conditions, modelled CO_2 concentrations were able to explain 71.1% and 76.1% (linear regression: $n = 8$, $p < .01$) of measured CO_2 variability under the observed DOC and high OC scenarios, respectively (Figure 7). Considering modelled aerobic respiration only, there was no significant difference between CO_2 concentrations near the surface of the GB, under the two OC scenarios (*t* test: $n = 9$, $t = 0.431$, $p = .672$). When we compared previously observed CO_2 evasion fluxes from the OSB (Boodoo et al., 2017) with those simulated under the observed DOC and high OC scenarios (Table 4), the modelled CO_2 evasion flux under the high OC scenario explained 57.3% ($n = 8$, $p < .05$) of observed CO_2 evasion flux variability

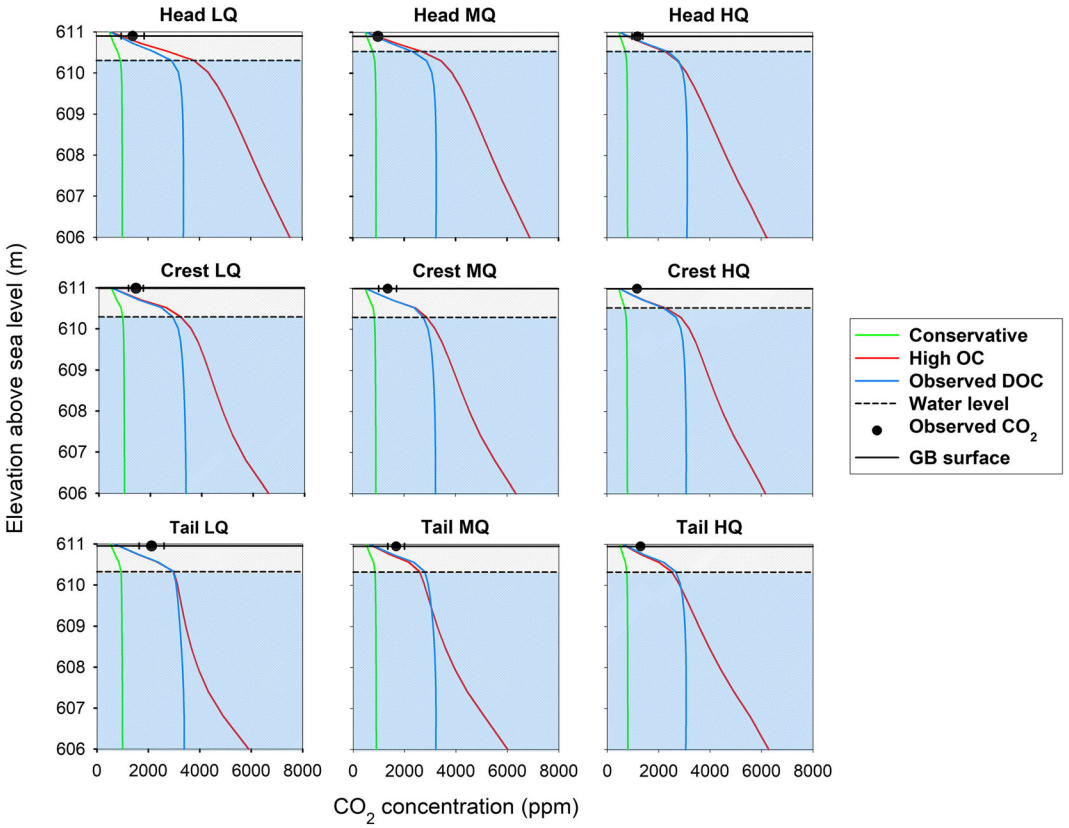

FIGURE 6 Change in modelled CO_2 concentration with depth below gravel bar (GB) surface under various dissolved organic carbon (DOC) scenarios (coloured lines) and different discharge-temperature conditions (LQ, MQ, and HQ; individual columns of subplots from left to right). The shaded circles and horizontal error bars represent the average and standard deviation of measured CO_2 concentrations at the respective locations and discharge-temperature conditions. The conservative scenario (green line) assumes downwelling of streamwater into the GB in the absence of aerobic respiration, whereas the blue and red lines represent scenarios in which aerobic respiration is limited and nonlimited, by DOC supply, respectively. The water level (dashed line) denotes the measured average water table of the GB during each sampling period. Details of CO_2 concentration (ppm) variability within the uppermost GB surface, near the water table boundary, are shown in Figure S2. OC, organic carbon

TABLE 4 Comparison of observed and modelled CO_2 evasion fluxes from the OSB GB under various discharge-temperature conditions

		LQ			MQ			HQ		
Variable	**Scenario/location**	**Head**	**Crest**	**Tail**	**Head[a]**	**Crest**	**Tail**	**Head**	**Crest**	**Tail**
CO_2 evasion flux ($mg\ C{\cdot}m^{-2}{\cdot}hr^{-1}$)	Observed GB	51.33	39.49	51.16	8.89	22.22	37.43	15.16	12.79	36.97
	Conservative model (streamwater downwelling)	3.87	4.34	6.41	3.56	3.84	5.26	2.86	2.69	3.14
	Modelled aerobic respiration (high OC)	22.93	19.16	22.69	17.64	14.46	15.94	16.14	16.91	15.36
	Modelled aerobic respiration (obs. DOC)	16.63	17.86	23.89	17.74	18.16	22.54	17.64	16.61	17.96
	Groundwater	11.67	0.44	9.78	1.87	0.41	3.70	0.89	0.13	0.63
	Zoobenthic respiration (single average estimate)	1.66	1.66	1.66	1.66	1.66	1.66	1.66	1.66	1.66
	CH_4 oxidization and other sources (high OC)	11.20	13.89	10.62	−15.84	1.85	10.87	−6.39	−8.60	16.18
	CH_4 oxidization and other sources (obs. DOC)	17.50	15.19	9.42	−15.94	−1.85	4.27	−7.89	−8.30	13.58
Measured CO_2 concentration (ppm)	Observed GB surface	1,404	1,442	2,124	979	1,358	1,671	1,188	1,174	1,292
	Observed streamwater downwelling	974	974	974	869	869	869	826	826	826
	Groundwater (estimated)[b]	3,105	3,105	3,105	2,422	2,422	2,422	1,465	1,465	1,465
Contribution to model CO_2 concentration (ppm)	Streamwater downwelling (conservative model)	616	628	664	605	603	629	569	551	577
	Modelled aerobic respiration (high OC)	351	257	366	350	241	322	255	236	308
	Modelled aerobic respiration (obs. DOC)	232	225	374	271	238	377	277	225	359
	Groundwater	319	16	406	206	25	165	70	12	22
	Zoobenthic respiration (single average estimate)	104	104	104	84	84	84	77	77	77
	CH_4 oxidization and other sources (high OC)	13	436	583	−266	405	471	217	298	309
	CH_4 oxidization and other sources (obs. DOC)	132	468	575	−187	408	416	195	309	258

Abbreviations: DOC, dissolved organic carbon; GB, gravel bar; OC, organic carbon.

[a]Data uncertain due to leak in CO_2 chambers during sampling.

[b]Groundwater CO_2 concentration was estimated as the maximum CO_2 concentration observed within the GB during each respective seasonal discharge-temperature sampling condition.

(Figure 7). Similarly, the observed DOC scenarios accounted for 50% (n = 8, p = .051) of CO_2 evasion flux variability. The fraction of the observed CO_2 evasion flux contributed by aerobic respiration ranged from 41% to 132% (Table 4).

Overall, 48.9% to 69.4% and 48.5% to 72.4% of the total observed variation in CO_2 concentrations could be explained by the sum of downwelling streamwater and aerobic respiration for observed DOC and high OC scenarios, respectively (Figure 7, Table 4). Modelled streamwater contributions accounted for 31.3% to 47.9% of the observed CO_2 concentrations (same for both scenarios). Aerobic respiration alone represented 15.6% to 27.8% and 17.2% to 25% of observed CO_2 concentration under the observed DOC and high OC scenarios, respectively (Table 4).

Although some of our modelled CO_2 evasion fluxes, particularly in winter, were overestimated, modelled aerobic respiration contribution to CO_2 concentration at the GB surface was in line with the findings of previous studies (Hotchkiss et al., 2015; Rasilo et al., 2017). In an analysis of 1,463 monitoring sites across the contiguous United States, where the internal CO_2 production accounted for 15% to 31% of the median CO_2 evasion flux. Furthermore, a reanalysis of the metabolism (Roberts et al., 2007) and CO_2 emissions (Jones & Mulholland, 1998) from a temperate forest stream, conducted by Hotchkiss et al. (2015), shows that aerobic respiration varied seasonally and ranged from 15% to 50% with the highest values occurring in autumn and the lowest in winter. Furthermore, in a study using a mass balance approach, Rasilo et al. (2017) found that DOC degradation accounted for 76% of all CO_2 evaded from their studied streams, with a large majority of CO_2 being produced within the hyporheic zone and transported to the stream where it outgasses.

4.6 | Further partitioning of CO_2 sources within the GB

Cumulatively, downwelled streamwater CO_2 and modelled aerobic respiration explained the major part (>50%) of the observed CO_2

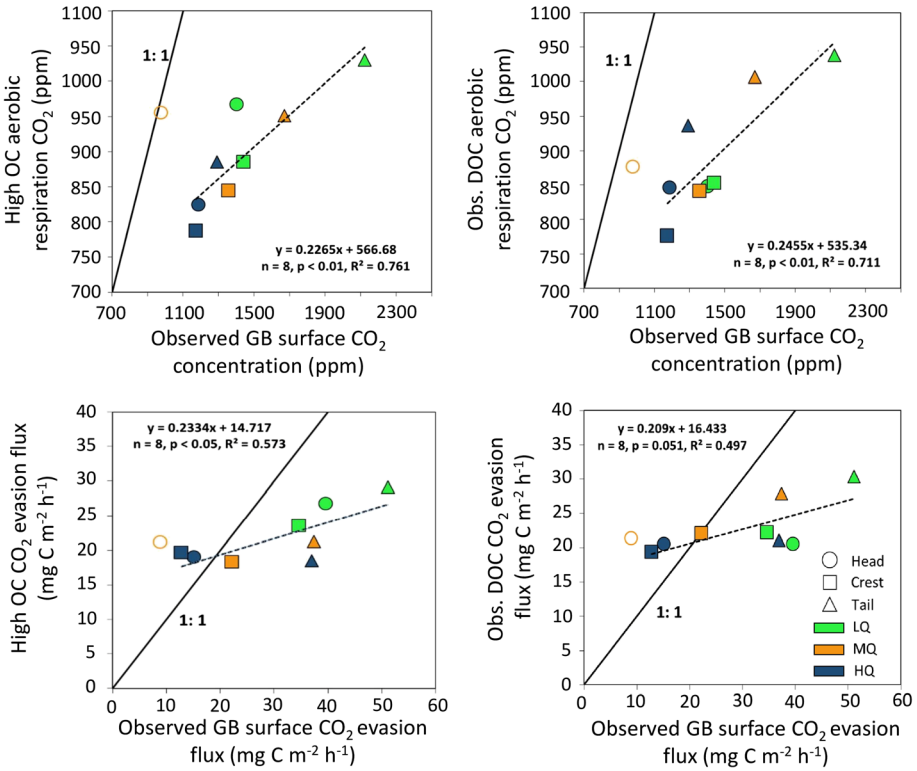

FIGURE 7 Modelled versus measured CO_2 concentration (a and b) and CO_2 evasion flux (c and d) along the head (circle), crest (square), and tail (triangle) of the gravel bar (GB) under different discharge-temperature conditions. Measured data points and horizontal error bars represent the average and standard deviation of diurnal measurements (three per day) over 6–7 consecutive days per location and discharge-temperature condition, respectively. The hollow circles represent measured CO_2 concentration (a and b) or evasion flux (c and d) during MQ at the head of the GB when a leak in the CO_2 flux chamber led to under-representation of actual CO_2 concentrations and evasion fluxes. These data were omitted for the calculation of the presented relationship. Linear regressions predicting aerobic respiration CO_2 concentration (a and b) and evasion flux (c and d) from observed CO_2 concentration and evasion flux at the GB surface are shown, in addition to the root mean squared deviation of MIN3P predicted aerobic CO_2 values from that of the linear model(s). DOC, dissolved organic carbon; OC, organic carbon

concentration at the GB surface across all location and scenarios (Figure 8). Residuals of CO_2 were highest at the GB tail, and lowest at the head, with residual contributions decreasing from LQ towards HQ. We estimated a single representative zoobenthic respiration CO_2 evasion flux of 1.66 mg C·m^{-2}·hr^{-1} (Supporting Information Text 4, Table S5), with a corresponding contribution to overall CO_2 concentration of 105 ppm (LQ), 84 ppm (MQ), and 77 ppm (HQ; Figure 8). Furthermore, on the basis of recent studies for the OSB (Boodoo et al., 2017; Peter et al., 2014) and estimates of streamwater–groundwater mixing using EC as a tracer (see Section 3), we calculated that groundwater accounted for another 1.0% to 22.7% of the observed CO_2 concentration at the GB surface. OSB groundwater CO_2 concentration was estimated to be 3.19, 2.79, and 1.77 times higher than that of the streamwater during LQ, MQ, and HQ, respectively (Table 4). Estimated groundwater influence was consistently higher at the head and tail as compared with the GB crest and decreased from LQ towards HQ (Tables 4 and S4). If these additional sources are taken into consideration, a residual term of 6% to 37% of the total CO_2 concentration remained over the three conditions at the various sampling locations (Table 4). The unexplained term was consistently lowest at the head of the GB, and differences in spatial variability across the GB sites decreased from LQ towards HQ (Figure 8).

Overall, considering GB averaged (head, crest, and tail) CO_2 concentration patterns across the three studied conditions, CO_2 concentrations decreased from LQ (1,657 ± 331 ppm), across MQ (1,515 ± 283 ppm), and towards HQ (1,218 ± 53 ppm; Table S6). Under the observed DOC scenario, the percentage contribution of GB aerobic respiration increased slightly from LQ (16.6% ± 0.8%), across MQ (20% ± 2.5%), and towards HQ (23.4% ± 3.5%). Meanwhile, considering no DOC limitation under the "high OC" scenario, DOC concentrations were relatively constant across the three studied conditions (20% ± 3.5% [LQ], 18.5% ± 0.8% [MQ], and 21.8% ± 1.5% [HQ]). Streamwater downwelling accounted for similar contributions during LQ (39.6% ± 5.9%) and MQ (41.0% ± 3.4%) and a higher contribution during HQ (46.5% ± 1.4%), whereas groundwater estimated contributions decreased steadily from LQ (14.3% ± 9.5%), across MQ (5.9% ± 4.0%), and towards HQ (2.9% ± 2.2%; Table S6).

We found that 91% to 98% (29% to 37%) of all incoming streamwater OC was respired and evaded as CO_2 under the observed DOC (high OC) scenario (Table 5). Carbon removal per unit stream length ranged from 0.23 to 0.24 g C·m^{-1}·hr^{-1} (0.36 to 0.45 g C·m^{-1}·hr^{-1}) across the entire width (43 m) and depth (3 m) of the model domain under the observed DOC (high OC) scenario (Table 5).

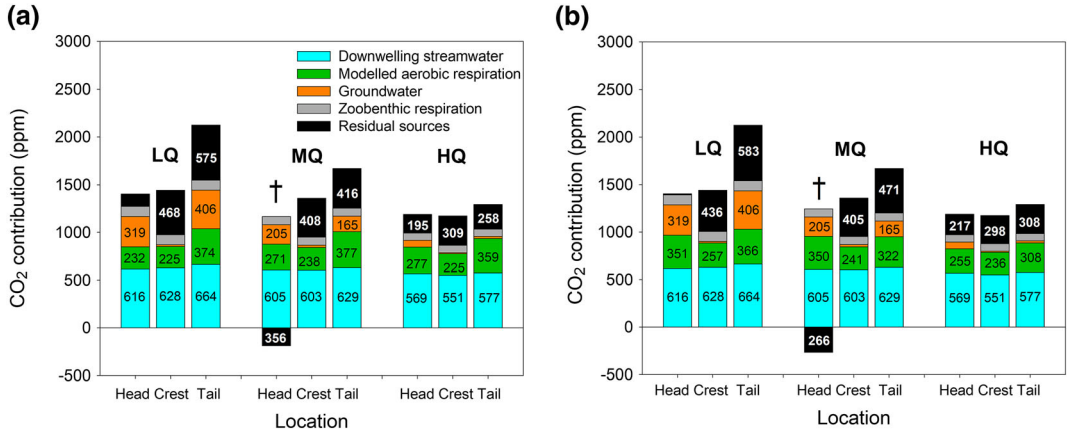

FIGURE 8 Partitioning of CO_2 sources along the gravel bar surface (head, crest, and tail) under varying discharge-temperature conditions for observed dissolved organic carbon (a) and high organic carbon (b) scenarios. Numbers in each bar represent the contribution of each source to the observed CO_2 concentration. Asterisks represent data with substantial uncertainty due to a leaky CO_2 flux chambers. †Data uncertain due to leak in CO_2 flux chambers during sampling

TABLE 5 Sources and sinks of CO_2 within OSB model domain

Model scenario	Condition	Influx (g C hr^{-1})	Outflux (g C hr^{-1})			Percentage C removal via outgassing	C removal per stream length via outgassing (g C·m^{-1}·hr^{-1})
			Surface CO_2 evasion flux	Groundwater	Downstream export		
Unlimited DOC	HQ	310.59	90.73	197.16	22.71	29.21	0.36
	MQ	278.16	99.00	146.51	32.65	35.59	0.39
	LQ	307.48	113.82	170.96	22.70	37.02	0.45
Limited DOC	HQ	66.24	60.28	4.61	1.35	91.00	0.24
	MQ	59.16	57.18	0.41	1.57	96.65	0.23
	LQ	64.89	63.48	0.36	1.06	97.82	0.25

Abbreviation: DOC, dissolved organic carbon.

5 | DISCUSSION

GBs have been recognized as hot spots for CO_2 outgassing, compared with their associated streams (Boodoo et al., 2017). They have been shown to cover a substantial percentage (5–26%) of the active channel surface area (Boodoo et al., 2017). However, the origin and underlying mechanisms of elevated CO_2 fluxes from GBs remain to date largely unclear. In order to better understand the sources and drivers of these fluxes, we modelled physical and biogeochemical processes, such as streamwater downwelling and aerobic respiration. We identified temperature and discharge as controls on GB CO_2 concentration and evasion fluxes. Our findings are in line with previous studies showing that these factors are also important for CO_2 fluxes from streams (Peter et al., 2014). Our findings further highlight the clear spatial variability of CO_2 concentrations and evasion at the surface of a GB. Spatial variability patterns were likely hydraulically driven and the result of higher water ages at the GB tail. Other studies have found distinct temporal variability, in terms of seasonal and diurnal CO_2 fluxes from the OSB stream, with higher streamwater evasion maxima occurring during the night and in summer as compared with during the day and in winter (Peter et al., 2014). These patterns are in line with our findings that overall CO_2 concentration and variability decreased with falling temperatures and increasing discharges.

Partitioning the CO_2 sources, we found that downwelling streamwater and aerobic respiration were the main sources of CO_2 to the GB subsurface, accounting for 31% to 48% and 17% to 36% of measured surface CO_2 concentrations, respectively. These major sources of CO_2 within the GB and likely their impact on CO_2 evasion fluxes are influenced by stream discharge and subsurface temperatures—factors directly impacted by climatic changes.

5.1 | Physicochemical and hydraulic patterns within the GB

We found the pattern of streamwater downwelling to control water age and flowpath lengths across the GB (Table 3). The observed pattern of initial decrease in water age with increasing depth (Figure 5) was likely the result of variation in the magnitude and origin of downwelling flowpaths. Partially submerged GBs experience changes in the flow field in terms of magnitudes and geometry with changes in stream discharge (Tonina & Buffington, 2007, 2011; Trauth et al., 2015). We found that shallow relatively slow flowpaths reach the

shallow observation points (d_{75}) whereas longer, high flowpath velocities dominate the deeper locations (d_{125}). These patterns are corroborated by measured physicochemical data where higher DO, and lower EC and subsurface temperatures that were more similar to that of the streamwater, was observed at the lower sampling depth (d_{125}), compared with that closer (d_{75}) to the GB surface (Table 3). Furthermore, the high variability of water age observed at the GB tail during LQ was likely the result of the mixing of substantially older water from the topographically lower side channel (Figure 1), with relatively younger streamwater downwelled along the main channel.

The EC signal within the shallow subsurface is predominantly a result of the mixing of streamwater (range 233–253 μS cm^{-1}) and groundwater (range 361–442 μS cm^{-1}) within the hyporheic zone (Vieweg et al., 2016). Higher groundwater influence was observed at the GB head and tail, compared with its crest, during LQ and MQ (Table 3). Groundwater commonly contains several times the concentration of dissolved CO_2 of the stream (e.g., ~4 times; Crawford et al., 2014), with a ratio of 1.77 to 3.19 at the OSB. These ratios are well within those found by Peter et al. (2014), when minimum observed streamwater and hyporheic pCO_2 levels are compared for their study of the OSB. Low volumes of groundwater can thus affect GB CO_2 concentration. As increased EC occurred in conjunction with increased observed CO_2 concentrations, it is likely that shallow groundwater contributed to CO_2 inputs within the GB. The drastic reduction in estimated groundwater CO_2 contribution during HQ is likely a result of the high levels of streamwater downwelling occurring during these conditions (Table 3) or the dilution of shallow groundwater by infiltrating snowmelt (HQ occurred in March) along the riparian zone. The latter is concurrent with observed lower groundwater EC and increased DO saturation during these conditions. Additionally, groundwater inputs may explain the overestimation of DO saturation by our model during LQ and MQ at the GB head and tail, as low DO groundwater mixes with more DO-rich streamwater within the subsurface, reducing overall DO.

5.2 | Aerobic respiration, CO_2 concentration, and evasion flux variability

Although the OSB stream can transiently act as a sink of atmospheric CO_2 (Peter et al., 2014), the OSB stream, and even more so the GB, acted as sources of atmospheric CO_2 during all conditions under which we conducted our samplings. Moreover, any decrease in CO_2 concentrations as a result of in-stream primary production would directly be introduced into the model as downwelling streamwater within the conservative model scenario. Downwelling streamwater contributed the major fraction of CO_2 to the subsurface of the GB and also to CO_2 evasion fluxes at the GB surface. Furthermore, higher fluxes from the GB as compared with the OSB streamwater were likely due to the higher concentration gradient between the GB surface and the atmosphere compared with at the streamwater–atmosphere interface. The observed pattern of the sudden shift in slope of CO_2 concentration versus depth upon approaching the fully saturated zone (Figure 6) is likely due to dispersive mixing within the saturated zone and the relatively rapid upward diffusion of CO_2 towards the GB surface through the air-filled pore spaces of the unsaturated zone.

On the basis of the observed DOC and high OC model scenarios, we were able to investigate the effect of DOC availability on aerobic respiration in the hyporheic zone. Considering the average observed DOC concentration across the three discharge-temperature scenarios (observed DOC scenario concentration: 1.26 mg L^{-1}) and corresponding model μ_{max} of 26.44 mg C·L^{-1}·day^{-1}, the potential DOC turnover time for the OSB is 0.048 days, which agrees very closely to that calculated values by Battin (1999), ~0.05 days. Thus, it is clear that the modelled near total removal of DOC under the observed DOC scenario is due to the relatively low DOC concentration of 1.26 mg L^{-1} measured within the GB. Furthermore, this suggests that other sources of DOC, such as particulate organic matter and biofilm exudates, may fuel in situ aerobic respiration within the OSB subsurface, as groundwater contributions to the GB subsurface and thus their DOC contribution to respiration were found to be low. Considering a high OC availability within the OSB subsurface (high OC scenario) and corresponding model μ_{max} of 1.31 mg C·L^{-1}·day^{-1}, we estimate a DOC turnover time for the OSB of 4.58 days. This is one order of magnitude higher than that estimated under the observed DOC scenario. Findlay, Strayer, Goumbala, and Gould (1993) reported a 50% removal of streamwater DOC concentration (~2.0 mg L^{-1}) within the hyporheic zone of a GB. This GB, however, had a sediment hydraulic conductivity (0.004 m s^{-1}) more than one order of magnitude lower than the OSB GB. A lower hydraulic conductivity would likely limit streamwater downwelling and lead to oxygen limitation further along the flowpaths, inhibiting aerobic respiration. In turn, this would indicate that within our GB, DO was not a limiting factor of aerobic respiration.

Whereas there was a significant difference in modelled CO_2 concentration in the deeper zone (>1.5 m) of the model between the two scenarios, the near-surface concentrations did not significantly differ (Figure 6). This lack of a significant difference in near-surface CO_2 indicates that the measured DOC concentration (1.26 mg L^{-1}), used for the observed DOC scenario, was not limiting within the shallow parts of the GB subsurface, facilitating similar levels of DOC consumption between the two scenarios. DOC concentrations became limiting at greater depths, leading to significantly higher CO_2 concentrations under the high OC scenario (DOC equivalent = 6.0 mg L^{-1}; Figure 6). Furthermore, occurrence of higher modelled aerobic CO_2 production under the observed DOC scenario, compared with that of the high OC, was due to the higher model maximum rate of reaction (26.04 mg C·L^{-1}·day^{-1}) applied under the observed DOC model scenario as the model rate of reaction compensates for observed DO saturation under the observed DOC concentration (1.26 mg L^{-1}).

Temperature affects reaction rates in accordance with the Arrhenius' equation, impacting subsurface aerobic microbial respiration and other subsurface biogeochemical processes (Munz, Oswald, & Schmidt, 2017; Zheng, Cardenas, & Wang, 2016). Low flowpath

velocities and increased residence time within the hyporheic zone are associated with increased biogeochemical processing and enhanced degradation of organic matter (Boano et al., 2014; Briggs, Lautz, & Hare, 2013; Gomez, Wilson, & Cardenas, 2012; Zarnetske, Haggerty, Wondzell, & Baker, 2011). Thus, the observed decreasing GB temperatures from LQ towards HQ (a change of −4.84°C) likely affected aerobic respiration reaction kinetics (Marzadri et al., 2012), with the rate decreasing with falling seasonal temperatures from LQ towards HQ. Likewise, increasing flowpath velocities from LQ towards HQ would lead to a gradual reduction in aerobic respiration as residence times are reduced. Decreasing spatial variability in CO_2 concentration within the GB in terms of modelled aerobic respiration from LQ towards HQ (Figure 8) was likely an effect of increasingly homogeneous hydraulic conditions, measured as flowpath velocity, across the GB (Table 3). Furthermore, the observed significant correlation between water age and CO_2 concentrations measured at d_{75} highlights the role of hydrology and flowpath origin in hyporheic reactions and CO_2 evasion fluxes. Therefore, it is likely that both seasonal temperature and discharge acted as major drivers of CO_2 production via aerobic respiration, with a corresponding decrease in DO consumption. Overall, we propose that aerobic microbial respiration in GBs is sensitive to changes in environmental variables, such as temperature and hydraulics.

Overall, GB averaged (head, crest, and tail) CO_2 concentrations and its spatial variability (measured as standard deviation) decreased from LQ towards HQ across the three studied conditions (Table S6). The observed pattern of increasing contribution of downwelling streamwater CO_2 and aerobic respiration (under the observed DOC scenario) from LQ towards HQ (Table S6) was likely hydrologically driven by increased downwelling velocity of streamwater into the GB (Table 3). This would also explain the decreased contribution of groundwater CO_2 to overall GB CO_2 concentration as the GB and surrounding streambed become increasingly losing from LQ towards HQ.

5.3 | Additional sources of CO_2 within GB

The hyporheic zone is an area of high zoobenthic density, with densities of >50,000 individuals m^{-3} reported for the OSB (Bretschko, 1991a, 1991b). As macrozoobenthic and meio-zoobenthic organisms within the streambed contribute to CO_2 production, zoobenthic respiration may account for an appreciable fraction of the CO_2 evasion flux. We estimated a small (~6% across all studied conditions) but relevant contribution of zoobenthic respiration to CO_2.

Further, oxidation of CH_4 from groundwater within the streambed along flowpaths towards the stream can represent a significant source of CO_2 within the hyporheic zone and stream (Hlaváčová et al., 2006; Krause et al., 2011; Rasilo et al., 2017). Rasilo et al. (2017) showed that several carbon species can coexist even under intermediate oxygen conditions (>40% saturation). We propose that CH_4 may act as a possible additional source of CO_2 in our study system, contributing to our CO_2 residual term. The short anoxic flowpath originating from the GB side channel during LQ, and possibly to a lesser extent at higher flow conditions, was possibly rich in CH_4 that may have become gradually oxidized to CO_2 en route to the GB tail.

5.4 | Limitations of study and reactive transport model

Our study corroborates the effect of in-stream GBs on stream subsurface hydrology, and reactions therein, by combining field measurements with numerical modelling (Munz et al., 2017; Shope et al., 2012; Trauth et al., 2015). Overall, the reactive transport model was able to simulate the OSB hydrology and oxygen dynamics reasonably well, with most points within 20% deviation from the observed data (Figures 4 and S1). Due to the homogeneous nature of our model, our results excluded any patterns originating from small localized heterogeneities in GB sediments. These could manifest as low conductivity patches resulting from the deposition of fine sediment during low flows (Bretschko, 1991a) or preferential flowpaths (Wagner & Bretschko, 2002). Such heterogeneities can in turn influence subsurface microbial processes (Nogaro, Datry, Mermillod-Blondin, Descloux, & Montuelle, 2010). Furthermore, as we applied steady-state models, effects of transient hydraulic and physiochemical conditions were not accounted for. This may contribute to some disagreement between modelled and observed CO_2 concentrations and fluxes—resulting from variability in water ages and flowpath lengths and changes in stream solute concentrations.

CO_2 evasion fluxes from streams to the atmosphere are a function of the gas transfer velocity, k_{CO2}, which typically increases with discharge, resulting in increased CO_2 evasion fluxes to the atmosphere (Peter et al., 2014). We estimated the k_{CO2} for the OSB stream, under the three different discharge-temperature scenarios in accordance with the methods used for the same stream by Peter et al. (2014). We found the k_{CO2} to be within the same order of magnitude (1.5×10^{-5} m s^{-1}, 6.0×10^{-5} m s^{-1}, and 7.5×10^{-5} m s^{-1} at LQ, MQ, and HQ, respectively). As we assumed Darcian flow within the GB subsurface, we expect that negligible turbulence and thus GB evasion fluxes were predominantly driven by CO_2 concentration gradients across the GB:air boundary. Furthermore, our MIN3P model utilizes CO_2 concentration as input, which is unaffected by stream turbulence. Finally, tethered floating chambers have been found to be subject overestimation of streamwater CO_2 evasion fluxes, as a result of enhanced turbulence at the upstream end of the chamber—leading to artificially higher CO_2 evasion fluxes within the chamber on turbulent streams (Lorke et al., 2015). However, assuming such an occurrence within our measurements would only underline the predominant role of GB evasion fluxes versus those of the OSB (Boodoo et al., 2017).

In a study conducted at the OSB, Battin (1999) found the rate of DOC removal within the stream subsurface to be the equivalent of 1.28 mg $C{\cdot}L^{-1}{\cdot}day^{-1}$, a value that represented ~1.4 times the measured DO removal, citing possible adsorption and temporary storage of DOC within subsurface biofilms. Our low modelled DO saturation levels, particularly during MQ and HQ, were likely the result of the assumption that all DO was removed via respiration, whereby 1 mol

of oxygen is removed per mole of DOC. Although anoxic conditions within the GB did not occur, such conditions may occur within the riparian zone and may contribute to groundwater CO_2, which is accounted for by the groundwater source component in our study.

The removal of DO via the oxidation of reduced species such as CH_4 originating from anoxic groundwater may also contribute to the underestimation of DO by the model. On the other hand, readily available additional sources of DOC may originate from the release of GB subsurface biofilm exudates or the degradation of Particulate Organic Carbon (POC) (Marx et al., 2017) originating from the GB side channel to DOC within the GB subsurface or direct inputs from DOC-rich shallow groundwater (Table 3). Modelled DOC concentration within the GB for the three different discharge-temperature conditions was kept constant. This was done as, though DOC concentration varied diurnally within the sampling periods, GB averaged DOC concentration (the overall average DOC concentration of the three GB locations during a sampling condition) among the different sampling conditions did not significantly differ (Table 2). As DOC variability is typically run-off induced on the event to seasonal scale (Fasching, Ulseth, Schelker, Steniczka, & Battin, 2016; Marx et al., 2017), it is possible that our imposed discharge restriction limits the transferability of our findings at times with high run-off dynamics.

Limited significant variability in CO_2 concentrations may have been the result of local hydrological driving factors being more significant than that resulting from the change in discharge over the studied scenarios (71–478 L s^{-1}). Additionally, the clear diurnal variability of CO_2 concentration and evasion fluxes, measured as the coefficient of variation (Table 3), particularly during LQ may mask variability in CO_2 across the different discharge-temperature scenarios at each GB location.

Further, it is possible that our model estimates of CO_2 concentration and fluxes, resulting from aerobic respiration, were slightly overestimated. Although measured DO saturation within the GB indicated that DO was not limiting, it is possible that this assumption may have led to an overestimation of aerobic respiration. This may be particularly the case during HQ, when in fact DO saturation was underestimated by the model at all locations (Figure 4). Modelled maximum aerobic respiration rates were calibrated to observed DO saturation, assuming that aerobic respiration was the only process of O_2 depletion within the GB. Although microbial aerobic respiration is a major process in the hyporheic zone consuming O_2 (Comer-Warner et al., 2018; Naegeli & Uehlinger, 1997), it is often accompanied by other processes consuming O_2 or releasing CO_2 within the hyporheic zone (e.g., nitrification along relatively short flowpaths, Zarnetske et al., 2011; and CH_4 oxidation to CO_2, Rasilo et al., 2017).

6 | CONCLUSIONS

We found spatial and temporal variability in CO_2 concentrations and evasion fluxes within a prealpine stream GB across three different discharge-temperature conditions. Utilizing a reactive transport model, we were able to disentangle the contribution of different sources to observed CO_2 concentration and resultant evasion fluxes from the GB, including streamwater downwelling and aerobic microbial respiration. Our model was able to explain ~70% and ~50% of the overall variability in CO_2 concentrations and evasion fluxes, with a root mean squared deviation of less than 10% and 15% of the model predicted values for CO_2, under the observed DOC and high OC scenarios, respectively. The relevant contribution of in situ subsurface aerobic respiration to GB CO_2 concentrations highlights the importance of this source for evasion. Furthermore, the variability in overall measured GB CO_2 concentration and the contribution of groundwater and residual sources among locations and across the different seasons, decreasing from LQ towards HQ, demonstrate the sensitivity of the different sources to changes in hydraulic conditions. Despite our model indicating strong downwelling across all sampling periods, we estimated groundwater to contribute only a minor but very variable fraction to overall GB CO_2 concentration (cf. Duvert et al., 2018). Similarly, zoobenthic respiration was found to act as a small but relevant source of CO_2 within the GB.

Using observed DOC and high OC scenarios for modelling aerobic respiration did not result in relevant differences in CO_2 dynamics at the surface of the GB. However, the two scenarios differed markedly in CO_2 concentrations at greater depth. The studied section of the OSB was losing, facilitating the transfer of streamwater towards the GB subsurface and potentially groundwater during all flow conditions. Therefore, we propose that DOC availability, its lability, and factors altering the aerobic respiration rate within the GB (such as temperature) will possibly alter the proportions of CO_2 exported to groundwater via the GB subsurface.

Climate change is expected to shift the run-off regimes of prealpine streams from snow dominated to rain dominated. This is predicted to increase winter discharge and the length of summer low flows (e.g., Barnett, Adam, & Lettenmaier, 2005). The occurrence of extended summer low flows would increase the overall exposure time and area of unsubmerged sections of GBs and potential for increased CO_2 evasion fluxes to the atmosphere. Although higher temperatures and increased residence times would provide the biophysical opportunity for increased respiration and other biogeochemical processes resulting in higher CO_2 fluxes, a source limitation of DOC within the GB, as occurred in our study under the observed DOC scenario, could limit GB aerobic respiration.

As we found CO_2 concentration and flux to increase with decreasing discharge and increasing temperature, it is possible that these changes could result in an increase of future overall GB CO_2 production and evasion flux. We provide a potentially first estimate of the source contributions to overall CO_2 concentrations and eventual evasion fluxes from GBs during a range of low discharge conditions. We highlight significant spatial and temporal variability at the feature scale (GBs), a common stream morphological feature, and the possible significance of GBs to evasion flux estimates from streams.

ACKNOWLEDGMENTS

This study received funding from European Union FP7 People: Marie-Curie Actions, Grant/ Award Number: 607150. We thank G.

Steniczka, H. Kraill, S. Schmid, C. Preiler, M. Mayr, C. Fasching, and M. Vanek for field and laboratory assistance; R. Poeppl and B. Groiss for assistance with topographical surveys and providing equipment; and Uli Maier for support in setting up MIN3P models.

ORCID

Kyle S. Boodoo https://orcid.org/0000-0001-7063-5042
Jakob Schelker https://orcid.org/0000-0002-0274-7605
Christian Schmidt https://orcid.org/0000-0001-9787-8327

REFERENCES

Aufdenkampe, A. K., Mayorga, E., Raymond, P. A., Melack, J. M., Doney, S. C., Alin, S. R., … Yoo, K. (2011). Riverine coupling of biogeochemical cycles between land, oceans, and atmosphere. *Frontiers in Ecology and the Environment*, *9*(1), 53–60. https://doi.org/10.1890/100014

Ayachit, U. (2015). *The ParaView guide: updated for ParaView version 4.3*. USA: Kitware Inc.

Barnett, T. P., Adam, J. C., & Lettenmaier, D. P. (2005). Potential impacts of a warming climate on water availability in snow-dominated regions. *Nature Reviews*, *438*(11), 303–309. https://doi.org/10.1038/nature04141

Bastviken, D., Sundgren, I., Natchimuthu, S., Reyier, H., & Gålfalk, M. (2015). Technical note: Cost-efficient approaches to measure carbon dioxide (CO2) fluxes and concentrations in terrestrial and aquatic environments using mini loggers. *Biogeosciences*, *12*, 3849–3859. https://doi.org/10.5194/bg-12-3849-2015

Battin, T. J. (1999). Hydrologic flow paths control dissolved organic carbon fluxes and metabolism in an alpine stream hyporheic zone. *Water Resources Research*, *35*(10), 3159–3169. https://doi.org/10.1029/1999WR900144

Battin, T. J., Luyssaert, S., Kaplan, L. A., Aufdenkampe, A. K., Richter, A., & Tranvik, L. J. (2009). The boundless carbon cycle. *Nature Geoscience*, *2*(9), 598–600. https://doi.org/10.1038/ngeo618

Boano, F., Harvey, J. W., Marion, A., Packman, A. I., Revelli, R., Ridolfi, L., & Wörman, A. (2014). Hyporheic flow and transport processes: Mechanisms, models, and biogeochemical implications. *Reviews of Geophysics*, *52*(4), 603–679. https://doi.org/10.1002/2012RG000417. Received

Boodoo, K. S., Trauth, N., Schmidt, C., Schelker, J., & Battin, T. J. (2017). Gravel bars are sites of increased CO2 outgassing in stream corridors. *Scientific Reports*, *7*(1), 14401. https://doi.org/10.1038/s41598-017-14439-0

Boulton, A. J., Datry, T., Kasahara, T., Mutz, M., & Stanford, J. A. (2010). Ecology and management of the hyporheic zone: Stream–groundwater interactions of running waters and their floodplains. *Journal of the North American Benthological Society*, *29*(1), 26–40. https://doi.org/10.1899/08-017.1

Bretschko, G. (1991a). The limnology of a low order alpine gravel stream (Ritrodat-Lunz study area). *Verh. Internat. Verein. Limnol.*, *24*, 1908–1912.

Bretschko, G. (1991b). Bed sediments, groundwater and stream limnology. *Verh. Internat. Verein. Limnol.*, *24*, 1957–1960.

Briggs, M. A., Lautz, L. K., & Hare, D. K. (2013). Residence time control on hot moments of net nitrate production and uptake in the hyporheic zone. *Hydrological Processes*, *28*(11), 3741–3751. https://doi.org/10.1002/hyp.9921

Campeau, A., & Del Giorgio, P. A. (2014). Patterns in CH4 and CO2 concentrations across boreal rivers: Major drivers and implications for fluvial greenhouse emissions under climate change scenarios. *Global Change Biology*, *20*(4), 1075–1088. https://doi.org/10.1111/gcb.12479

Cardenas, M. B., & Wilson, J. L. (2007). Dunes, turbulent eddies, and interfacial exchange with permeable sediments. *Water Resources Research*, *43*(8). https://doi.org/10.1029/2006WR005787

Chen, X. (2000). Measurement of streambed hydraulic conductivity and its anisotropy. *Environmental Geology*, *39*(12), 1317–1324. https://doi.org/10.1007/s002540000172

Comer-Warner, S. A., Romeijn, P., Gooddy, D. C., Marchant, B., Hannah, D. M., Krause, S., … Kettridge, N. (2018). Thermal sensitivity of CO2 and CH4 emissions varies with streambed sediment properties. *Nature Communications*, *9*, 2803. https://doi.org/10.1038/s41467-018-04756-x

Crawford, J. T., Lottig, N. R., Stanley, E. H., Walker, J. F., Hanson, P. C., Finlay, J. C., et al. (2014). CO2 and CH4 emissions from streams in a lake-rich landscape: Patterns, controls, and regional significance. *Global Biogeochemical Cycles*, *28*, 197–210. https://doi.org/10.1002/2013GB004661.Received

Cussler, E. L. (1997). *Diffusion: Mass Transfer in Fluid Systems*. Cambridge University Press. Retrieved from. https://books.google.de/books?id=TGRmfTrsPTQC

Drake, T. W., Raymond, P. A., & Spencer, R. G. M. (2017). Terrestrial carbon inputs to inland waters: A current synthesis of estimates and uncertainty. *Limnology and Oceanography Letters*, *3*, 132–142. https://doi.org/10.1002/lol2.10055

Duvert, C., Butman, D. E., Marx, A., Ribolzi, O., & Hutley, L. B. (2018). CO2 evasion along streams driven by groundwater inputs and geomorphic controls. *Nature Geoscience*, *11*(November), 813–818. https://doi.org/10.1038/s41561-018-0245-y

Fasching, C., Ulseth, A. J., Schelker, J., Steniczka, G., & Battin, T. J. (2016). Hydrology controls dissolved organic matter export and composition in an Alpine stream and its hyporheic zone. *Limnology and Oceanography*, *61*(2), 558–571. https://doi.org/10.1002/lno.10232

Findlay, S., Strayer, D., Goumbala, C., & Gould, K. (1993). Metabolism of streamwater dissolved organic carbon in the shallow hyporheic zone. *Limnology and Oceanography*, *38*(7), 1493–1499. https://doi.org/10.4319/lo.1993.38.7.1493

Finlay, J. C. (2003). Controls of streamwater dissolved inorganic carbon dynamics in a forested watershed. *Biogeochemistry*, *62*(3), 231–252. https://doi.org/10.1023/A:1021183023963

Gelhar, L. W., Welty, C., & Rehfeldt, K. R. (1992). A critical review of data on field-scale dispersion in aquifers. *Water Resources Research*, *28*(7), 1955–1974. https://doi.org/10.1029/92WR00607

Gomez, J. D., Wilson, J. L., & Cardenas, M. B. (2012). Residence time distributions in sinuosity-driven hyporheic zones and their biogeochemical effects. *Water Resources Research*, *48*(9), n/a–n/a. https://doi.org/10.1029/2012WR012180

Gómez-Gener, L., Obrador, B., Marcé, R., Acuña, V., Catalán, N., Casas-Ruiz, J. P., … von Schiller, D. (2016). When water vanishes: Magnitude and regulation of carbon dioxide emissions from dry temporary streams. *Ecosystems*, *19*(4), 710–723. https://doi.org/10.1007/s10021-016-9963-4

Grant, G., Burkholder, B., Jefferson, A., Lewis, S., & Haggerty, R. (2006). *Hyporheic flow, temperature anomalies, and gravel augmentation: Preliminary findings of a field investigation on the Clackamas River, Oregon*. Corvallis: Oregon State University, Report to Portland General Electric.

Grimm, N. B., & Fisher, S. G. (1984). Exchange between interstitial and surface water: Implications for stream metabolism and nutrient cycling. *Hydrobiologia*, *111*, 219–228. https://doi.org/10.1007/BF00007202

Gu, C., Hornberger, G. M., Mills, A. L., Herman, J. S., & Flewelling, S. A. (2007). Nitrate reduction in streambed sediments: Effects of flow and biogeochemical kinetics. *Water Resour. Res*, *43*, W12413.

Hlaváčová, E., Rulík, M., Čáp, L., & Mach, V. (2006). Greenhouse gas (CO2, CH4, N2O) emissions to the atmosphere from a small lowland stream in Czech Republic. *Archiv für Hydrobiologie*, *165*(3), 339–353. https://doi.org/10.1127/0003-9136/2006/0165-0339

Hotchkiss, E. R., Hall Jr, R. O., Sponseller, R. A., Butman, D., Klaminder, J., Laudon, H., … Karlsson, J. (2015). Sources of and processes controlling CO2 emissions change with the size of streams and rivers. *Nature Geoscience*, *8*(9), 696–699. https://doi.org/10.1038/ngeo2507

Hvorslev, M. J. (1951). *Time lag and soil permeability in groundwater observations*. Waterways Experiment Station, Vicksburg, Mississippi: U.S. Army Corps of Engineers.

IPCC (2013). In T. F. Stocker, D. Qin, G.-K. Plattner, M. Tignor, S. K. Allen, J. Boschung, et al. (Eds.), *Climate Change 2013: The Physical Science Basis. Contribution of Working Group I to the Fifth Assessment Report of the Intergovernmental Panel on Climate Change* (p. 1535). Cambridge, United Kingdom and New York, NY, USA: Cambridge University Press.

Jones, J. B., & Mulholland, P. J. (1998). Influence of drainage basin topography and elevation on carbon dioxide and methane supersaturation of stream water. *Biogeochemistry*, *40*(1), 57–72. https://doi.org/10.1023/A:1005914121280

Kasahara, T., & Hill, A. R. (2008). Lateral hyporheic zone chemistry in an artificially constructed gravel bar and a re-meandered stream channel, Southern Ontario, Canada. *Journal of the American Water Resources Association*, *43*(5), 1257–1269. https://doi.org/10.1111/j.1752-1688.2007.00108.x

Kasahara, T., & Wondzell, S. M. (2003). Geomorphic controls on hyporheic exchange flow in mountain streams. *Water Resources Research*, *39*(1), SBH 3-1–SBH 3-14. https://doi.org/10.1029/2002WR001386

Krause, S., Hannah, D. M., Fleckenstein, J. H., Heppell, C. M., Kaeser, D., Pickup, R., … Wood, P. J. (2011). Inter-disciplinary perspectives on processes in the hyporheic zone. *Ecohydrology*, *4*(4), 481–499. https://doi.org/10.1002/eco

Lapierre, J. F., Guillemette, F., Berggren, M., & Del Giorgio, P. A. (2013). Increases in terrestrially derived carbon stimulate organic carbon processing and CO_2 emissions in boreal aquatic ecosystems. *Nature Communications*, *4*. https://doi.org/10.1038/ncomms3972

Lauerwald, R., Laruelle, G. G., Hartmann, J., Ciais, P., & Regnier, P. A. G. (2015). Spatial patterns in CO2 evasion from the global river network. *Global Biogeochemical Cycles*, *29*(5), 534–554. https://doi.org/10.1002/2014GB004941. Received

Looman, A., Maher, D. T., Pendall, E., Bass, A. M., & Santos, I. R. (2017). The carbon dioxide evasion cycle of an intermittent first-order stream: Contrasting water–air and soil–air exchange. *Biogeochemistry*, *1–2*(June), 87–102. https://doi.org/10.1007/s10533-016-0289-2

Lorke, A., Bodmer, P., Noss, C., Alshboul, Z., Koschorreck, M., Somlai-Haase, C., … Premke, K. (2015). Technical note: drifting versus anchored flux chambers for measuring greenhouse gas emissions from running waters. *Biogeosciences*, *12*(23), 7013–7024. https://doi.org/10.5194/bg-12-7013-2015

Maier, U., DeBiase, C., Baeder-Bederski, O., & Bayer, P. (2009). Calibration of hydraulic parameters for large-scale vertical flow constructed wetlands. *Journal of Hydrology*, *369*(3), 260-273. https://doi.org/https://doi.org/10.1016/j.jhydrol.2009.02.032

Marx, A., Dusek, J., Jankovec, J., Sanda, M., Vogel, T., van Geldern, R., … Barth, J. A. C. (2017). A review of CO2 and associated carbon dynamics in headwater streams: A global perspective. *Reviews of Geophysics*, *55*(2), 560–585. https://doi.org/10.1002/2016RG000547

Marzadri, A., Tonina, D., & Bellin, A. (2012). Morphodynamic controls on redox conditions and on nitrogen dynamics within the hyporheic zone: Application to gravel bed rivers with alternate-bar morphology. *Journal of Geophysical Research*, *117*, G00N10. https://doi.org/10.1029/2012JG001966

Marzadri, A., Tonina, D., & Bellin, A. (2013). Effects of stream morphodynamics on hyporheic zone thermal regime. *Water Resources Research*, *49*(4), 2287–2302. https://doi.org/10.1002/wrcr.20199

Mayer, K. U., Frind, E. O., & Blowes, D. W. (2002). Multicomponent reactive transport modeling in variably saturated porous media using a generalized formulation for kinetically controlled reactions. *Water Resources Research*, *38*(2), 13-1–13-21. https://doi.org/10.1029/2001WR000862

Munz, M., Oswald, S. E., & Schmidt, C. (2017). Coupled long-term simulation of reach-scale water and heat fluxes across the river-groundwater interface for retrieving hyporheic residence times and temperature dynamics. *Water Resources Research*, *53*(11), 8900–8924. https://doi.org/10.1002/2017WR020667

Naegeli, M. W., & Uehlinger, U. (1997). Contribution of the hyporheic zone to ecosystem metabolism in a prealpine gravel-bed-river. *Journal of the North American Benthological Society*, *16*(4), 794–804. https://doi.org/10.2307/1468172

Nogaro, G., Datry, T., Mermillod-Blondin, F., Descloux, S., & Montuelle, B. (2010). Influence of streambed sediment clogging on microbial processes in the hyporheic zone. *Freshwater Biology*, *55*(6), 1288–1302. https://doi.org/10.1111/j.1365-2427.2009.02352.x

Norman, F. A., & Cardenas, M. B. (2014). Heat transport in hyporheic zones due to bedforms: An experimental study. *Water Resources Research*, *50*(4), 3568–3582. https://doi.org/10.1002/2013WR014673. Received

Peter, H., Singer, G. A., Preiler, C., Chifflard, P., Steniczka, G., & Battin, T. J. (2014). Scales and drivers of temporal pCO2 dynamics in an Alpine stream. *Journal of Geophysical Research, Biogeosciences*, *119*, 1078–1091. https://doi.org/10.1002/2013JG002552

R Core Team. (2017). R Development Core Team. *R: A language and environment for statistical computing*, *55*, 275–286. http://www.R-project.org

Rasilo, T., Hutchins, R. H. S., Ruiz-González, C., & del Giorgio, P. A. (2017). Transport and transformation of soil-derived CO2, CH4 and DOC sustain CO2 supersaturation in small boreal streams. *Science of the Total Environment*, *579*, 902–912. https://doi.org/10.1016/j.scitotenv.2016.10.187

Raymond, P. A., Hartmann, J., Lauerwald, R., Sobek, S., Mcdonald, C., Hoover, M., … Kortelainen, P. (2013). Global carbon dioxide emissions from inland waters. *Nature*, *503*, 355–359. https://doi.org/10.1038/nature12760

Roberts, B. J., Mulholland, P. J., & Hill, W. R. (2007). Multiple Scales of Temporal Variability in Ecosystem Metabolism Rates: Results from 2 Years of Continuous Monitoring in a Forested Headwater Stream. *Ecosystems*, *10*(4), 588–606. https://doi.org/10.1007/s10021-007-9059-2

Schelker, J., Singer, G. A., Ulseth, A. J., Hengsberger, S., & Battin, T. J. (2016). CO2 evasion from a steep, high gradient stream network: Importance of seasonal and diurnal variation in aquatic pCO2 and gas transfer. *Limnology and Oceanography*, *61*(5), 1826–1838. https://doi.org/10.1002/lno.10339

von Schiller, D., Marcé, R., Obrador, B., Gómez-Gener, L., Casas-Ruiz, J. P., Acuña, V., & Koschorreck, M. (2014). Carbon dioxide emissions from dry watercourses. *Inland Waters*, *4*, 377–382. https://doi.org/10.5268/IW-4.4.746

Schnitzer H, Streicher W, Steininger KW, Berger T, Brunner C, Passer A, Schneider J, Titz M, Trimmel H, Türk A. 2014. *Austrian panel on climate change (APCC)—Austrian assessment report 2014* (*AAR14*). Available at: http://hw.oeaw.ac.at/7699-2

Shope, C. L., Constantz, J. E., Cooper, C. A., Reeves, D. M., Pohll, G., & McKay, W. A. (2012). Influence of a large fluvial island, streambed, and stream bank on surface water-groundwater fluxes and water table dynamics. *Water Resources Research*, *48*(6), W06512. https://doi.org/10.1029/2011WR011564

Tonina, D., & Buffington, J. M. (2007). Hyporheic exchange in gravel bed rivers with pool-riffle morphology: Laboratory experiments and three-dimensional modeling. *Water Resources Research*, *43*(1), 1–16. https://doi.org/10.1029/2005WR004328

Tonina, D., & Buffington, J. M. (2011). Effects of stream discharge, alluvial depth and bar amplitude on hyporheic flow in pool-riffle channels. *Water Resources Research*, *47*(8), 1–13. https://doi.org/10.1029/2010WR009140

Trauth, N., Schmidt, C., Maier, U., Vieweg, M., & Fleckenstein, J. H. (2013). Coupled 3-D stream flow and hyporheic flow model under varying stream and ambient groundwater flow conditions in a pool-riffle system. *Water Resources Research*, *49*(9), 5834–5850. https://doi.org/10.1002/wrcr.20442

Trauth, N., Schmidt, C., Vieweg, M., Maier, U., & Fleckenstein, J. H. (2014). Hyporheic transport and biogeochemical reactions in pool-riffle systems under varying ambient groundwater flow conditions. *Journal of Geophysical Research, Biogeosciences*, *119*(5), 910–928. https://doi.org/10.1002/2013JG002586.Received

Trauth, N., Schmidt, C., Vieweg, M., Oswald, S. E., & Fleckenstein, J. H. (2015). Hydraulic controls of in-streamgravel bar hyporheic exchange and reactions. *Water Resources Research*, *51*, 2243–2263. https://doi.org/10.1002/2014WR015857.Received

Vieweg, M., Kurz, M. J., Trauth, N., Fleckenstein, J. H., Musolff, A., & Schmidt, C. (2016). Estimating time-variable aerobic respiration in the streambed by combining electrical conductivity and dissolved oxygen time series. *Journal of Geophysical Research, Biogeosciences*, *121*, 2199–2215. https://doi.org/10.1002/2016JG003345.Received

Wagner, F. H., & Bretschko, G. (2002). Interstitial flow through preferential flow paths in the hyporheic zone of the Oberer Seebach, Austria. *Aquatic Sciences*, *64*, 307–316. https://doi.org/10.1007/s00027-002-8075-8

Ward, N. D., Keil, R. G., Medeiros, P. M., Brito, D. C., Cunha, A. C., Dittmar, T., … Richey, J. E. (2013). Degradation of terrestrially derived macromolecules in the Amazon River. *Nature Geoscience*, *6*(7), 530–533. https://doi.org/10.1038/ngeo1817

Zarnetske, J. P., Haggerty, R., Wondzell, S. M., & Baker, M. A. (2011). Dynamics of nitrate production and removal as a function of residence time in the hyporheic zone. *Journal of Geophysical Research*, *116*(G1). https://doi.org/10.1029/2010JG001356

Zheng, L., Cardenas, M. B., & Wang, L. (2016). Temperature effects on nitrogen cycling and nitrate removal-production efficiency in bedform-induced hyporheic zones. *Journal of Geophysical Research, Biogeosciences*, *121*(4), 1086–1103. https://doi.org/10.1002/2015JG003162

SUPPORTING INFORMATION

Additional supporting information may be found online in the Supporting Information section at the end of the article.

How to cite this article: Boodoo KS, Schelker J, Trauth N, Battin TJ, Schmidt C. Sources and variability of CO_2 in a prealpine stream gravel bar. *Hydrological Processes*. 2019;33:2279–2299. https://doi.org/10.1002/hyp.13450